

1 **Diabatic Eddy Forcing Increases Persistence and Opposes Propagation**
2 **of the Southern Annular Mode in MERRA2**

3 Pending revision at *Journal of Atmospheric Science*. Copyright in this work may be
4 transferred without further notice.

5

6 Samuel Smith,^{a,b} Jian Lu,^c and Paul W. Staten^b

7 ^a *University of Chicago, Chicago, IL*

8 ^b *Indiana University, Bloomington, IN*

9 ^c *Pacific Northwest National Laboratory, Richland, WA*

10

11 *Corresponding author:* Samuel Smith; samuelsmith@uchicago.edu

13

ABSTRACT

14 As a dominant mode of jet variability on sub-seasonal timescales, the Southern
15 Annular Mode (SAM) provides a window into how the atmosphere can produce internal
16 oscillations on longer-than-synoptic timescales. While SAM's existence can be explained by
17 dry, purely barotropic theories, the timescale for its persistence and propagation is set by a
18 lagged interaction between barotropic and baroclinic mechanisms, making the exact physical
19 mechanisms challenging to identify and to simulate, even in latest generation models. By
20 partitioning the eddy momentum flux convergence in the MERRA2 reanalysis using an eddy-
21 mean flow interaction framework, we contend that diabatic processes, such as condensation
22 and radiative heating, are the main contributors to SAM's persistence in its stationary regime,
23 as well as the key for preventing propagation in this regime. In SAM's propagating regime,
24 baroclinic and diabatic feedbacks also dominate the eddy-jet feedback. However, propagation
25 is initiated by barotropic shifts in upper-level wave-breaking and then sustained by a
26 baroclinic response, leading to a roughly 60-day oscillation period. This barotropic
27 propagation mechanism has been identified in dry, idealized models, but here we show
28 evidence of this mechanism for the first time in reanalysis. The diabatic feedbacks on SAM
29 are consistent with modulation of the storm track latitude by SAM, altering the emission
30 temperature and cloud cover over individual waves. Therefore, we suggest that any attempts
31 to improve SAM representation in models must consider the influence of storm track
32 location, as well as cloud and moisture parameterizations.

33

SIGNIFICANCE STATEMENT

34 As they circumnavigate the planet, the tropospheric jet streams slowly drift north and
35 south over about 30 days, longer than the normal limit of weather prediction. Understanding
36 the source of this "memory" could improve our knowledge of how the atmosphere organizes
37 itself and our ability to make long-term forecasts. Current theories have identified several
38 possible internal atmospheric interactions responsible for this memory. Yet most of the
39 theories for understanding the jets' behavior assume that this behavior is only weakly
40 influenced by atmospheric water vapor. We show that this assumption is not enough to
41 understand jet persistence. Instead, clouds and precipitation are more important contributors
42 in reanalysis data than internal "dry" mechanisms to this memory of the Southern
43 Hemisphere jet.

44

45 **1. Introduction**

46 The most ubiquitous modes of variability in extratropical zonal winds are the
47 barotropic “annular” modes, subseasonal to interannual fluctuations in tropospheric jet
48 latitude which evoke a contracting and dilating annulus (Rossby and Willet 1948; Kidson
49 1988a; Thompson and Wallace 2000; Thompson et al. 2000). These annular dynamics are
50 generated by a coherent shift of upper-tropospheric wave breaking and an associated shift of
51 the eddy momentum flux convergence (EMFC) which drives the barotropic jets (Thompson
52 and Wallace 2000; Lorenz and Hartmann 2001). Even highly idealized atmospheric models
53 can reproduce the essential ingredients of annular modes (Lee and Feldstein 1996; Barnes et
54 al. 2010; Lutsko and Hell 2021), evidence that they are both fundamental and theoretically
55 established.

56 Given their low-frequency variability, barotropic annular modes (hereafter, annular
57 modes) have been identified as a potential source of predictability in the atmosphere at
58 longer-than-synoptic timescales (Kidson 1988b; Baldwin and Dunkerton 2001; Son and Lee
59 2006). Such efforts, however, have been complicated by difficulties in accurately simulating
60 the annular mode timescale (Gerber et al. 2008), which is over-predicted even in latest
61 generation models (Bracegirdle et al. 2020). Moreover, these model timescale biases have
62 implications beyond predictability. Although there is much debate, these biases may imply an
63 overestimation of the jet response to external forcing (Gritsun and Branstator 2007; Ring and
64 Plumb 2008; Kidston and Gerber 2010; but also, Simpson and Polvani 2016; Hassanzadeh
65 and Kuang 2016).

66 Perhaps the foremost mechanism to explain annular mode persistence is a positive
67 eddy-jet feedback (Robinson 2000, Lorenz and Hartmann 2001; Simpson et al. 2013; Nie et
68 al. 2014; Ma et al. 2017; Lubis and Hassanzadeh 2020). The clearest evidence for the
69 feedback is a positive correlation between the anomalous jet latitude and the annular-mode-
70 induced EMFC seven to ten days later (Lorenz and Hartmann 2001). However, the feedback
71 does not appear in all seasons, and it is plausible that the proximate eddy-jet feedback is a
72 manifestation of low-frequency variability, perhaps by way of the stratosphere (Byrne et al.
73 2016; Saggioro and Shepherd 2019). Nonetheless, eddy-jet feedbacks have been
74 unambiguously demonstrated in idealized models forced with annular mode anomalies (Ma et
75 al. 2017).

76 Another potential mechanism explains the increased persistence of annular modes
77 through an interaction between the jet-shifting and jet-pulsing modes of variability (Lubis and
78 Hassanzadeh 2020), typically defined as the first and second empirical orthogonal functions
79 (EOFs) of zonal-mean zonal wind. While the two EOFs are uncorrelated at short lags (by
80 construction), at longer lags, an equatorward shift of the jet is often preceded by a weakened
81 jet and followed by a stronger jet. This interaction produces a slow meridional propagation of
82 zonal wind anomalies (Lee et al. 2007; Sheshadri and Plumb 2017), and it explains the
83 decreased annular mode timescale during propagation relative to the stationary regime (Lubis
84 and Hassanzadeh 2020). Further, the decorrelation timescales of both EOFs can be predicted
85 across all lags using only a single lag in the propagating system (Sheshadri and Plumb 2017),
86 highlighting the coupled dynamics of the modes.

87 Given the endurance of timescale biases across model generations (Gerber et al. 2008;
88 Simpson and Polvani 2016; Bracegirdle et al. 2020), improving the representation of annular
89 mode timescales will require capturing higher-order dynamics than those represented in dry,
90 idealized models. For example, recent work has suggested that the presence of moisture acts
91 variously as a positive feedback on annular modes by selectively damping high-frequency
92 eddies which shorten jet persistence (Lutsko and Hell 2021), or a negative feedback through
93 the reduction of zonal-mean baroclinicity (Xia and Chang, 2014).

94 Beyond the effects of condensational heating, cloud radiative effects (CRE) have also
95 been suggested to affect the annular mode timescale because high clouds respond to shifts in
96 the Southern Hemisphere jet (Thompson and Wallace 2000, Liu et al. 2020). Yet it remains
97 unclear how CRE might feed back on the annular modes. Li et al. (2014) suggest CRE might
98 decrease the annular mode timescale in the Northern Hemisphere, but Papavasileiou et al.
99 (2020) find CRE weakly increase the timescale of its regional manifestation, the North
100 Atlantic Oscillation. Notably, Papavasileiou et al. (2020) find significant positive feedbacks
101 from latent heating and clear-sky heating on the North Atlantic Oscillation.

102 Since diabatic heating can influence EOF1 variability, it suggests diabatic heating
103 may also influence the propagation of annular mode anomalies. In idealized models, radiative
104 damping of large-scale eddies is partially responsible for the meridional propagation of zonal
105 wind anomalies (Lee et al. 2007). In this model, propagation is primarily a barotropic
106 process driven by slow shifts in the critical latitude for wave breaking. However, other
107 idealized models suggest a balance between baroclinic processes and radiative damping drive

108 propagation (Sparrow et al. 2009). The relative contributions of baroclinic, barotropic, and
109 diabatic processes to the propagation of annular mode anomalies have yet to be determined.

110 The relative balance between processes for stationary modes of variability is also
111 unclear. Upper-level barotropic shifts feedback onto the low-level baroclinicity, which
112 increases in response to the enhanced surface friction and which helps maintain the upper-
113 level anomaly (Robinson 2000; Blanco-Fuentes and Zurita-Gotor 2011; Zurita-Gotor et al.
114 2014). Diabatic heating damps this baroclinic response by modifying the low-frequency eddy
115 forcing; suggesting an important but unclear role (Zurita-Gotor et al. 2014; Lutsko and Hell
116 2021). Nie et al. (2014; henceforth N14) attempt to resolve this using an eddy-mean flow
117 interaction framework. However, their finding of primarily barotropic feedbacks neglects
118 diabatic heating entirely, despite their framework's ability to quantify these impacts (Huang
119 and Nakamura 2016).

120 The present work aims to address the following two questions. **First**, we seek to
121 clarify the relative contributions of diabatic and other processes to the stationary regime in
122 reanalysis data of the Southern Hemisphere, which has been the focus of many previous
123 efforts to quantify eddy-jet feedbacks (Lorenz and Hartmann 2001; Simpson et al. 2013;
124 N14) due to its relative zonal symmetry. **Second**, we examine the relative contributions of
125 diabatic, baroclinic, and barotropic processes for the propagating regime of SAM variability.
126 This further motivates examining SAM, as it exhibits both stationary and propagating
127 regimes depending on the season (Sheshadri and Plumb, 2017; and Figure 2).

128 Using different seasons as proxies for stationary and propagating regimes of SAM, we
129 apply an eddy-mean flow interaction framework extended from the work of N14 to show that
130 diabatic heating is the largest source of the eddy-jet feedback and the largest opposition to
131 propagation in December-February (DJF). Additionally, baroclinic feedbacks, followed
132 closely by diabatic feedbacks, are most important during March-November for the
133 decorrelation timescale, while propagation is driven barotropically. Further, this work shows
134 that the diabatic feedback in DJF is principally from clear-sky heating, while latent heating is
135 more significant for the propagating regime in March-November. These diabatic feedbacks
136 are likely a result of a shift in the latitude of wave generation with the jet, resulting in warmer
137 and wetter eddies for equatorward jet shifts and colder and drier eddies for poleward jet
138 shifts.

139 The rest of the work is outlined as follows. We begin by reviewing the finite-
 140 amplitude wave activity (FAWA) theory which allows us to quantify the contributions of
 141 diabatic heating to the combined pseudomomentum and mean flow (Nakamura and Zhu
 142 2010), highlighting where our analysis improves upon N14. We then outline our
 143 methodology based on a partitioning of the EMFC. The results of this partitioning are
 144 presented first, followed by an analysis of where and how diabatic feedbacks are operating.
 145 We conclude with some reflections on utilizing our methodology as a part of a strategy to
 146 determine the source of model biases.

147 2. Theory

148 A simple budget for SAM results from the vertically integrated, zonal-mean zonal
 149 momentum balance in quasi-geostrophy (Lorenz and Hartmann, 2001; N14):

$$150 \quad \frac{d\langle \bar{u} \rangle}{dt} = \langle M \rangle - \overline{X}_s \quad (1)$$

151 Where u is the zonal momentum, M is the EMFC, X_s is boundary-layer friction, the overbar
 152 represent the zonal-mean, and the angle brackets $\langle \cdot \rangle$ represents vertical (mass-weighted)
 153 integration over the depth of the troposphere (1000-100hPa). The EMFC, M , is given by

$$154 \quad M \equiv -\frac{1}{a \cos^2 \phi} \frac{\partial}{\partial \phi} (\overline{u'v'} \cos^2 \phi),$$

155 where the prime represents deviations from the zonal-mean, ϕ is latitude, a is the planetary
 156 radius, and v is meridional velocity. Notably, the EMFC in the extratropics is predominantly
 157 confined to be above 500hPa and primarily geostrophic; thus, we can also write

$$158 \quad \frac{d\langle \bar{u} \rangle}{dt} \approx \gamma \langle M \rangle_{500} - \overline{X}_s \equiv \gamma \langle M_g \rangle_{500} + \gamma \langle M_a \rangle_{500} - \overline{X}_s. \quad (2)$$

159 Now the integration of M is over 500-100hPa, and we introduce a scale factor $\gamma \equiv \frac{4}{9}$, given
 160 the relative mass of the upper troposphere to the entire troposphere (Lorenz 2023). M_g is the
 161 geostrophic EMFC defined identically to M except utilizing the geostrophic wind, i.e.,

$$162 \quad M_g \equiv -\frac{1}{a \cos^2 \phi} \frac{\partial}{\partial \phi} (\overline{u'_g v'_g} \cos^2 \phi).$$

163 $M_a \equiv M - M_g$ is thus the ageostrophic component of M , and it is retained for reasons that
 164 will become evident. As in N14, we choose to focus on upper-level momentum because 1)

165 the anomalous EMFC associated with SAM is concentrated above 500hPa, 2) SAM is
 166 understood as primarily barotropic, and 3) this division enables us to separately understand
 167 contributions from the lower troposphere.

168 To further probe SAM dynamics, we make use of the FAWA framework for eddy-
 169 mean flow interaction (Nakamura and Zhu 2010). FAWA applies a contour integral operator
 170 to quasi-geostrophic (QG) potential vorticity (PV) q_g to quantify the pseudomomentum
 171 contained in large-scale eddies. FAWA (A) measures the amplitude of large-scale Rossby
 172 wave packets by integrating over the displacement of a PV anomaly from a conservative
 173 zonal symmetry (Q)

$$174 \quad A \equiv A^S + A^N \equiv \frac{a}{2\pi \cos \phi_e} \iint_{\substack{q > Q \\ \phi \leq \phi_e}} q_g \cos \phi d\lambda d\phi - \frac{a}{2\pi \cos \phi_e} \iint_{\substack{q \leq Q \\ \phi > \phi_e}} q_g \cos \phi d\lambda d\phi. \quad (3)$$

175 Here, ϕ_e is the equivalent latitude, the latitude an anomaly would have in conservative zonal
 176 symmetry. This zonal symmetry is found by dividing southward and northward PV
 177 displacements into regions of equal area, i.e., such that the area poleward of ϕ_e is equivalent
 178 to the area poleward of the PV contour it bisects. Thus, FAWA is an area-preserving
 179 integration. See Nakamura and Zhu (2010) or Huang and Nakamura (2016) for more detail.

180 In Eq. (3), A^S and A^N are wave activity from southward contour displacements and
 181 northward displacements, respectively. In the Southern Hemisphere, A^S is wave activity from
 182 large-scale anticyclonic waves ($q - Q > 0$), and A^N is from cyclonic waves ($q - Q < 0$).
 183 Because $A \geq 0$ by construction, contrary to some definitions, we define both A^S and A^N as
 184 similarly non-negative, functionally absorbing the difference in Eq. (3) into A^N .

185 Applying the integral operator in Eq. (3) to the PV budget results in a budget for wave
 186 activity (see Nakamura and Zhu 2010 and Nakamura and Solomon 2010 for derivations;
 187 compare to N14; Lu et al. 2015; Palipane et al. 2017)

$$188 \quad \frac{\partial A}{\partial t} = -\overline{v'_g q'_g} - K_{eff}^e \frac{1}{a} \frac{\partial Q}{\partial \phi} + \Delta \Sigma. \quad (4)$$

189 The subscript g indicates the geostrophic component of the wind, $\Delta \Sigma$ represents diabatic and
 190 nonconservative sources of wave activity, and K_{eff}^e is the effective eddy diffusivity,
 191 representing the enhancement of the small-scale diffusive sink of wave activity by the large
 192 scale stretching of the material PV contour. K_{eff}^e must be diagnosed residually from Eq. (4).

193 Importantly, N14 assumes that $\Delta\Sigma$ is negligible to compute K_{eff}^e , given that diabatic
 194 heating is much smaller in the upper troposphere than the lower. However, we show that $\Delta\Sigma$
 195 is not negligible, as coincidence between diabatic heating and upper-level waves enables
 196 diabatic injection of PV and subsequent modification of wave activity. This has significant
 197 consequences for the calculation of K_{eff} and the conclusions of N14, as we will show in
 198 section 4a.

199 The diabatic contributions to FAWA ($\Delta\Sigma$) are found by applying the integral operator
 200 in Eq. (3) to the PV source generated by differential vertical heating from diabatic sources
 201 (c.f. Andrews 1987, Palipane et al. 2017), or

$$202 \quad \Delta\Sigma \equiv \frac{a}{2\pi \cos \phi_e} \left\{ \iint_{\substack{q>Q \\ \phi \leq \phi_e}} f \frac{\partial}{\partial p} \left[\frac{(p_R p^{-1})^\kappa}{c_p d\tilde{\theta}/dp} J_T \right] \cos \phi d\lambda d\phi - \iint_{\substack{q \leq Q \\ \phi > \phi_e}} f \frac{\partial}{\partial p} \left[\frac{(p_R p^{-1})^\kappa}{c_p d\tilde{\theta}/dp} J_T \right] \cos \phi d\lambda d\phi \right\} \quad (5)$$

203 κ is the Poisson constant, c_p is the specific heat capacity at constant pressure, $p_R =$
 204 1000 hPa is the reference pressure, and $J_T \equiv J_{LH} + J_{CRE} + J_{CS}$ is the total diabatic heating
 205 rate, computed as the sum of individual heating rates output by the reanalysis due to
 206 condensation, cloud longwave and shortwave radiation, and clear-sky longwave and
 207 shortwave radiation. As with wave activity A , $\Delta\Sigma$ can be decomposed into cyclonic and
 208 anticyclonic contributions, keeping the same sign convention as discussed previously ($\Delta\Sigma \equiv$
 209 $\Delta\Sigma^S + \Delta\Sigma^N$). $\Delta\Sigma$ can also be computed for the individual heating rates separately.

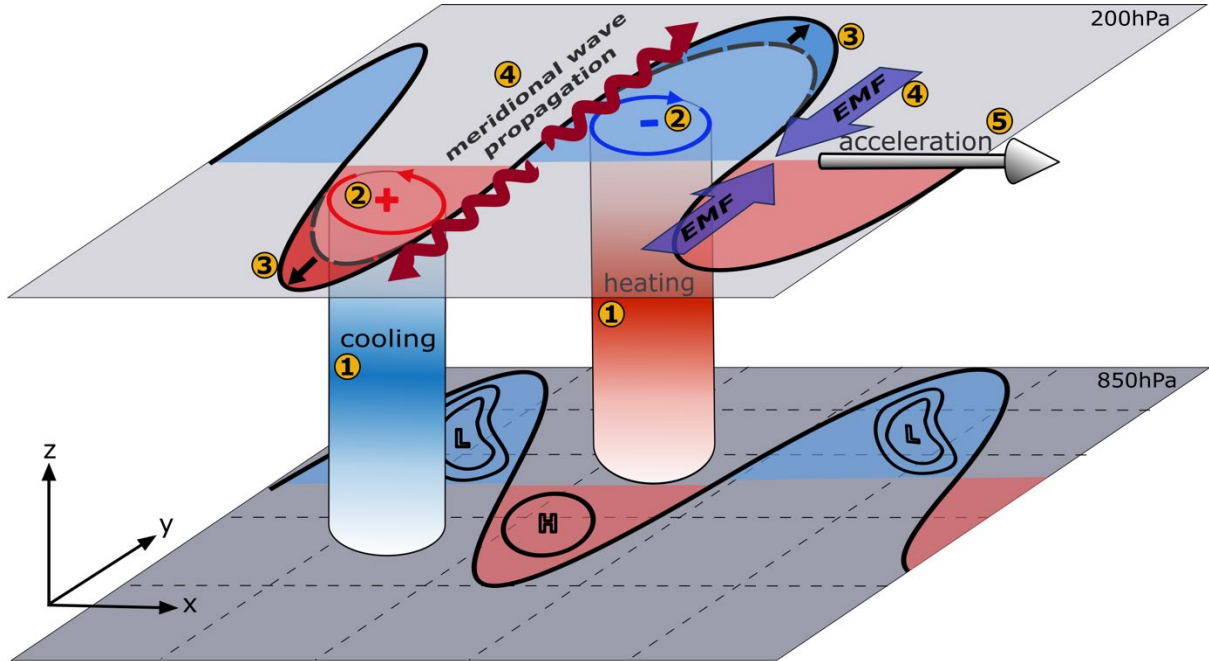
210 Eq. (5) can be scaled into a form identical to the vertical component of the Eliassen-
 211 Palm (EP) flux (see Supplemental Materials), and thus, physically, diabatic heating generates
 212 momentum in a similar process to the baroclinic injection of momentum. This is illustrated
 213 schematically in Figure 1. Diabatic heating (1) generates PV through differential heating akin
 214 to the stretching contributions to PV (2). By injecting anomalous cyclonic PV into cyclonic
 215 waves, or anticyclonic PV into anticyclonic waves, or vice versa, diabatic heating generates
 216 or removes wave activity (3). If the wave activity injection by diabatic heating propagates
 217 meridionally, then it induces an EMFC (4), which accelerates or decelerates the zonal wind
 218 (5).

219 Making use of the QG approximation that the meridional PV flux [first term on the
 220 rhs of Eq. (4)] balances the EP flux divergence, and also integrating vertically over the upper-
 221 troposphere (500-100hPa), we can transform Eq. (4) to elucidate the connection between
 222 wave activity and zonal wind,

223

$$\frac{\partial \langle A \rangle_{500}}{\partial t} = -\langle M_g \rangle_{500} - f \left(\frac{\overline{v'_g \theta'}}{d\tilde{\theta}/dp} \right) \Big|_{500} - \langle K_{eff}^e \rangle_{500} \frac{1}{a} \frac{\partial \langle Q \rangle_{500}}{\partial \phi} + \langle \Delta \Sigma \rangle_{500}. \quad (6)$$

224 Here θ represents potential temperature, $\tilde{\theta}(p)$ its hemispheric-mean value, and f is the
225 Coriolis parameter.



226 Fig. 1. Schematic depicting the diabatic injection of momentum in the Southern Hemisphere..
227 See text for full description.
228

230 Multiplying Eq. (6) by the scale factor γ , we can combine it with Eq. (2) to produce a
231 budget for the total momentum and wave activity,

232

$$\frac{d}{dt} (\langle \bar{u} \rangle + \gamma \langle A \rangle_{500}) = \gamma \langle M_a \rangle_{500} - \gamma f \left(\frac{\overline{v'_g \theta'}}{d\tilde{\theta}/dp} \right) \Big|_{500} - \gamma \langle K_{eff}^e \rangle_{500} \frac{1}{a} \frac{\partial \langle Q \rangle_{500}}{\partial \phi} + \gamma \langle \Delta \Sigma \rangle_{500} - \overline{X_s}. \quad (7)$$

233 If one integrates Eq. (7) over the entire troposphere, the meridional heat flux from the
234 boundary layer is balanced by the surface wave activity B , and it becomes (ignoring M_a)

235

$$\frac{d}{dt} (\langle \bar{u} \rangle + \langle A \rangle + B) = \dot{A} + \dot{B} - \overline{X_s},$$

236 where \dot{A} represents the combined effects of all nonconservative (diabatic and dissipative)
237 sources/sinks of wave activity and \dot{B} are sources/sinks of surface wave activity (e.g., surface
238 heat fluxes), in agreement with Wang and Nakamura (2015). Note that in the absence of
239 nonconservative processes, the quantity $(\langle \bar{u} \rangle + \langle A \rangle + B)$ is conserved, making FAWA (A) a

kind of pseudomomentum that has a tight inverse relationship with zonal momentum, akin to the relationship between available potential energy and kinetic energy in the energetic perspective. The negative covariation between FAWA and zonal wind is quite strong, even extending to a local conservation of pseudomomentum, particularly within storm track regions (Huang and Nakamura 2017, Nakamura and Huang 2018). Because of this tight connection, we will henceforth refer to pseudomomentum and FAWA interchangeably.

Thus, we can use Eq. (7) in the context of SAM to understand its evolution.

Furthermore, when $\frac{\partial}{\partial t} \langle A \rangle_{500} \approx 0$, particularly during the eddy feedbacks which set SAM's timescale, we can partition the EMFC to understand the relative contributions of each process, akin to the partitioning first done by N14, but now more completely. Because of the strong inverse connection between FAWA and zonal momentum, N14 further argue that the negative wave activity tendency $\left(-\frac{\partial A}{\partial t}\right)$ can be construed as transient momentum fluctuations which do not feedback (or only weakly feedback) on the mean flow, akin to the stochastic portion of the EMFC \tilde{m} of Lorenz and Hartmann (2001).

Thus, by comparing Eq. (7) with Eq. (1), we may partition the EMFC controlling SAM's dynamics as

$$\langle M \rangle_{500} = \underbrace{-\frac{\partial \langle A \rangle_{500}}{\partial t}}_{\text{transient}} - \underbrace{f \left(\frac{\overline{v'_g \theta'}}{d\tilde{\theta} dp} \right)_{500}}_{\text{baroclinic}} - \underbrace{\left\langle K_{eff}^e \frac{1}{a} \frac{\partial Q}{\partial \phi} \right\rangle}_{\text{barotropic}}_{500} + \underbrace{\langle \Delta \Sigma \rangle_{500}}_{\text{diabatic}} + \langle M_a \rangle_{500}. \quad (8)$$

Eq. (8) represents the decomposition for the EMFC into transient, barotropic, baroclinic, diabatic, and ageostrophic components. We drop the scale factor γ as all terms are integrated over the upper troposphere.

It should be noted here that Eq. (8) is a diagnostic equation, and that when the transient term $\left(-\frac{\partial \langle A \rangle}{\partial t}\right)$ is nonzero, we cannot determine the extent to which fluctuations in the EMFC are driving changes in FAWA or changes in FAWA are inducing a shift in the

263 EMFC through the horizontal radiation of Rossby waves¹. Further, as a diagnostic
264 partitioning of the EMFC, one should not interpret the results of Eq. (8) as stating that
265 removal of one of the processes on the rhs (such as in a dry or barotropic model) would
266 remove an equal amount of momentum. Rather, Eq. (8) reveals the relative contributions of
267 different processes in the highly-coupled eddy-mean flow interaction problem containing
268 exactly those processes. Thus, understanding how Eq. (8) evolves during the lifecycle of
269 SAM reveals insights into the relative importance of said processes determining its
270 underlying dynamics. The climatological mean of Eq. (8) for MERRA2 is shown in
271 Supplemental Figure 1.

272 The final step in utilizing Eq. (8) to analyze SAM is to project it onto SAM, following
273 Simpson et al. (2013) and N14. Thus, we partition SAM's evolution and feedbacks by the
274 various physical processes

275 $m_{up} = m_A + m_{bt} + m_{bc} + m_{db} + m_{ag}$. (9)

276 m_A is the contribution from the (negative) wave activity tendency, m_{bt} the contribution from
277 large-scale dissipation of FAWA through irreversible mixing (i.e., wave breaking), m_{bc} the
278 baroclinic contribution from the meridional eddy heat flux from the lower troposphere, m_{db}
279 the diabatic contribution, and m_{ag} the ageostrophic ones. Eq. (9) is projected onto SAM
280 because it allows us to utilize the framework of Lorenz and Hartmann (2001), found by
281 projecting Eq. (2) onto the SAM

282
$$\frac{dz}{dt} \approx \gamma m_{up} - \frac{z}{\tau}$$

283 Here z is the SAM index, and the second term on the rhs results from parameterizing the
284 frictional damping of SAM as Rayleigh damping at the boundary layer with timescale τ .

¹ It is worth noting, however, that Huang and Nakamura (2017) find a stronger covariation between FAWA and zonal momentum than between either FAWA and EMFC or zonal wind and EMFC, suggesting that the EMFC is not a principal driver of FAWA.

285 Finally, m_{db} can be further decomposed into various contributions as

286
$$m_{db} \equiv m_{LH} + m_{LWCS} + m_{LWCRE} + m_{SWCRE} + m_{SWCS} \quad (10a)$$

287
$$m_{db} \equiv m_{LH}^S + m_{LH}^N + m_{LWCS}^S + m_{LWCS}^N + m_{LWCRE}^S + m_{LWCRE}^N + m_{SWCRE}^S + m_{SWCRE}^N + m_{SWCS}^S + m_{SWCS}^N \quad (10b)$$

288 Here, subscripts on m denote the contribution from latent heating (LH), longwave clear-sky
289 heating (LWCS), longwave cloud radiative heating (LWCRE), shortwave clear-sky heating
290 (SWCS), and shortwave cloud radiative heating (SWCRE). Superscripts denote diabatic
291 contributions in anticyclonic waves (S) and cyclonic waves (N).

292 3. Data & Methods

293 3a. SAM Budget Analysis

294 Following Simpson et al. (2013) and N14, we take the SAM indices as the first two
295 EOFs of vertically-integrated, zonal-mean zonal wind, including the area-based weighting of
296 EOFs (Baldwin et al. 2009). We then project the wave activity budget onto each EOF spatial
297 basis as $m = \mathbf{M} \cdot (\mathbf{W} \mathbf{e}_{1,2}) \left\| \mathbf{W}^{\frac{1}{2}} \mathbf{e}_{1,2} \right\|^{-1}$, where \mathbf{M} is a component of the budget, \mathbf{W} is the
298 weight matrix, and $\mathbf{e}_{1,2}$ are the EOF spatial patterns. We then perform lead-lag regressions of
299 the projected terms onto the EOF timeseries ($z_{1,2}$). Decay timescales for each EOF are
300 estimated by fitting an exponential curve to each autoregression. Lag-dependent timescales τ
301 are estimated assuming an exponential decay of the autoregression ($C_{zz} \sim e^{-t/\tau}$) as $\tau \sim -$
302 $1/(d \ln C_{zz} / dt)^{-1}$ after smoothing the derivative with a 7-point running mean (Zurita-Gotor
303 et al. 2014). SAM feedbacks are calculated also following Simpson et al. (2013) and N14, as
304 the ratio between the regression slope of each $m_{1,2}$ to the regression slope of $u_{1,2}$, which is
305 the projection of u onto each EOF in the same manner.

306 PV is computed based on the full wind rather than only its geostrophic component, or
307 $q_g \equiv (a \cos \phi)^{-1} [\partial_\lambda(v \cos \phi) - \partial_\phi(u \cos \phi)] + f \left\{ 1 + \partial_p [(\theta - \tilde{\theta})(d_p \tilde{\theta})^{-1}] \right\}$ (c.f.
308 Nakamura and Solomon 2010). This decision improves the numerical issues with computing
309 the geostrophic wind (dividing by $\cos \phi$ in subtropics/tropics, strong height gradients near the
310 surface/topography) and results in a cleaner computation of wave activity based on q_g as
311 described below. This choice does not strongly impact our results (see section 4a).

312 Wave activity integrations described above are carried out through a careful, geo-
313 located sorting of the PV field to find the zonally-symmetric reference PV, followed by a grid

314 cell counting procedure to determine the displacement. Diabatic PV source fields are
315 integrated over the same area, akin to the process for column-water vapor of Smith et al.
316 (2021). PV source fields are computed using the integrand in Eq. (5) from diabatic heating
317 rates taken directly from the reanalysis output (see section 3c).

318 A composite of propagating events is made following a modification of the procedure
319 outlined in Lee et al. (2007; see their section 4). We identify middle times of candidate events
320 as any time where zonal wind anomalies are a local maximum at 50°S. Local maxima are
321 identified as the maxima during a period beginning when the wind anomalies at 50°S are
322 greater than 1 standard deviation above the mean and ending when anomalies have dipped
323 below that value for at least three days. To remove propagation events that have anomalously
324 short periods, the only local maxima retained must be a local maximum over a 70-day period
325 centered on the candidate maximum. The remaining local maxima are taken to be the middle
326 times of propagating events, of which we identify 81.

327 Ninety-percent confidence intervals for each budget term are produced via
328 bootstrapping. We generate 1000 random subsets of budget timeseries data (consecutively,
329 with replacement) of length 2555 days (~7 years). All regressions are performed with each
330 subset, selecting the 5th and 95th percentiles of the subsets as confidence interval bounds.

331 *3b. Analysis of breaking waves*

332 We further investigate the physical mechanisms behind diabatic influences on SAM
333 through an analysis of nonlinear, breaking waves. Waves are identified here as regions above
334 the 90th percentile for a given month in both cyclonic and anticyclonic wave activity
335 separately, located between 25°-75°S. Identified regions must also be at least 500,000 km² in
336 size to remove small-scale contributions to wave activity.

337 After computing the center of mass of a large wave activity region, we interpolate all
338 fields to a 3000 km x 3000 km locally Cartesian grid centered at the wave activity centroid
339 (given in *equivalent* latitude) to capture the entire wave region. Fields are averaged over the
340 domain and vertically from 500-100hPa for all identified wave events, and then regressed
341 against the year-round SAM (EOF1) index.

342 *3c. Data Source*

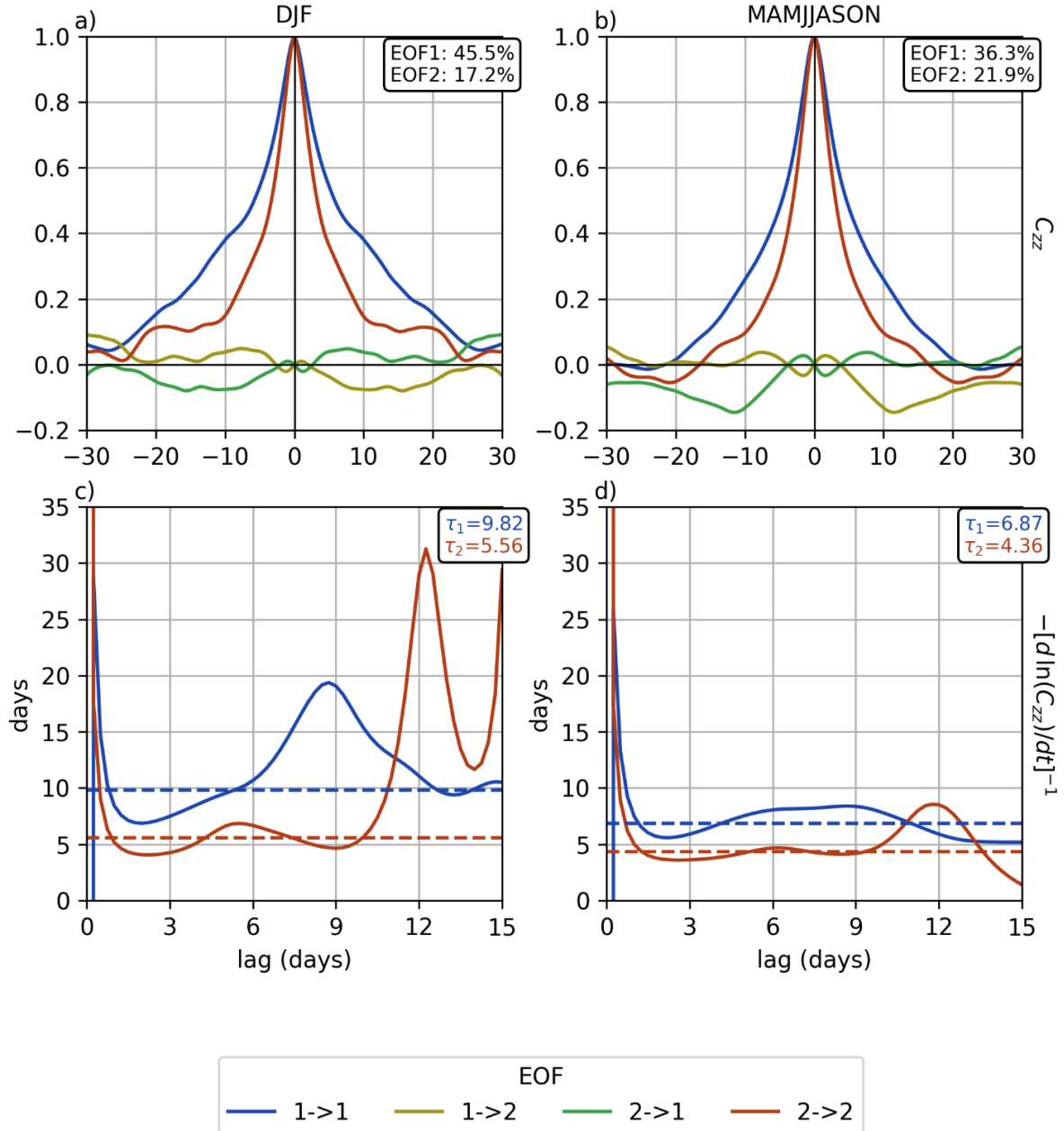
343 Data for this work are obtained from NASA MERRA2 reanalysis. MERRA2 data are
344 gridded at approximately 0.5° latitude by 0.625° longitude resolution, with 29 vertical levels
345 between surface and mid-stratosphere (30hPa). Further details can be found in Gelaro et al.
346 (2017). MERRA2 was chosen for this work because it provides different diabatic heating
347 rates and fast accessibility. Due to storage constraints, a recent 15 years of 6-hourly data,
348 2005-2019, were selected. These high-frequency data are needed to resolve medium-scale
349 waves (periods around 2 days) which contribute to SAM (Ma et al. 2017). Because we can
350 identically reproduce N14's results, which utilized a different and longer dataset (see
351 Supplemental Figure 2), we do not expect that our choice of dataset or temporal range are
352 strongly impacting our results.

353 Data downloaded are horizontal velocity, geopotential height, temperature, surface
354 pressure, and temperature tendencies due to longwave, longwave clear-sky, shortwave,
355 shortwave clear-sky, and moist processes. Cloud heating rates are diagnosed simply as all-sky
356 rates minus clear-sky rates.

357 **4. Results & Discussion**

358 *4a. SAM Pseudomomentum Budgets*

359 We begin our discussion by recognizing that SAM exhibits different behavior in
360 different seasons (Sheshadri and Plumb 2017; also Figure 2). MAMJJASON shows all the
361 hallmarks of propagation: 1) cross-correlations between EOF1 and EOF2, 2) a similar decay
362 timescale between EOFs 1 and 2, and 3) a similar fraction of variance explained by both
363 EOFs (Lee et al. 2007; Sheshadri and Plumb 2017; Lubis and Hassanzadeh 2020). In
364 contrast, DJF shows: 1) weak cross-EOF correlations, 2) an EOF1 timescale almost double
365 that of EOF2, and most importantly, 3) more than twice the variance explained by EOF1 than
366 by EOF2. [The threshold ratio for discriminating between regimes is 2:1, see Lee et al.
367 (2007).] Physically, the stationary regime is associated with single jet climates when the
368 eddy-driven jet is weak, such as during summer, and the propagating regime tends to form
369 when the eddy-driven jet is stronger and displaced from the subtropical jet, as in most of the
370 rest of the year (Lee et al. 2007). We proceed using DJF as a proxy for the stationary regime,
371 and MAMJJASON as a proxy for the propagating regime. (Data are de-seasonalized before
372 examining their relationship with SAM.)



373

374 Fig. 2. Lead-lag regressions of EOF 1 and 2 timeseries of zonal-wind onto themselves and
375 each other, for a) December-January (DJF) and b) March-November (MAMJJASON) from
376 2005-2019 in MERRA2. Also listed is the variance explained by each mode (normalized
377 eigenvalue). The bottom row shows the smoothed, implied decorrelation timescale (assuming
378 exponential decay) for the EOF 1 and 2 autocorrelations as a function of lag (solid lines) for
379 c) DJF and d) MAMJJASON, as well as the mean decorrelation timescale produced by fitting
380 an exponential decay function to the autocorrelations in panels a) and b).

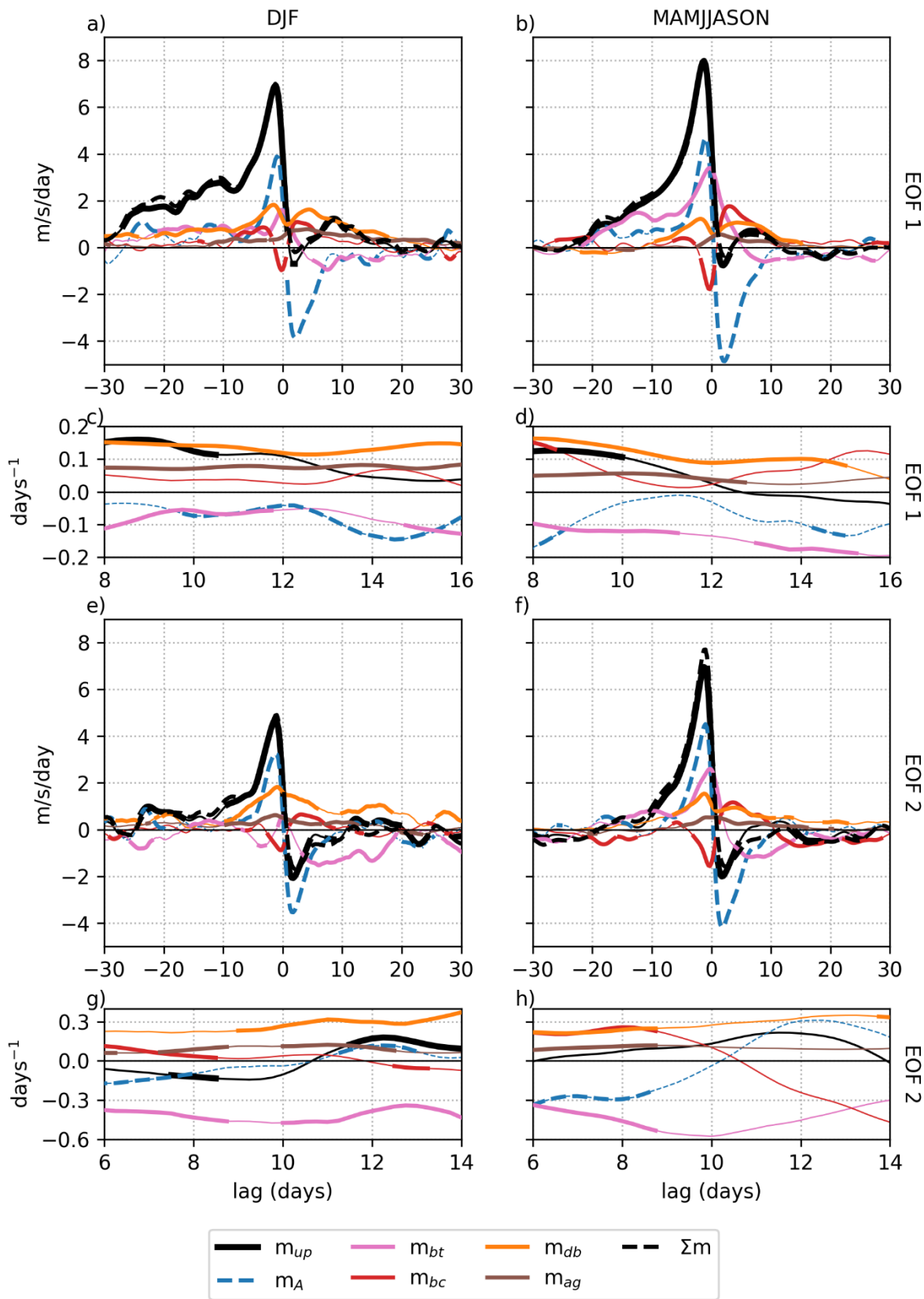
381

382 Based on the implied decorrelation timescale (solid lines in Figure 2c,d), we focus on
383 processes at lag day 10 throughout this analysis. This results from a compromise between the
384 different peaks in feedbacks for EOFs 1 (day 9) and 2 (day 12) and the need to avoid the

385 stochastic forcing of synoptic eddies at short timescales and the weak correlations at long
386 lags. We also consider that positive feedbacks are predominantly active where the
387 decorrelation timescales are longer than SAM's frictional damping timescale of ~7-8 days
388 (Lorenz and Hartmann 2001, Zurita-Gotor 2014, Lubis and Hassanzadeh 2020). Finally, we
389 aim to capture the interactions between EOFs, which peak around day 10 for MAMJJASON.
390 While choosing to focus on a single lag day of 10 results in EOF2 feedbacks that are
391 somewhat weak, it greatly simplifies the analysis by enabling consideration of feedbacks and
392 propagation simultaneously.

393 Prior to lag day zero during the generation of EOFs 1 and 2, SAM is primarily
394 barotropic and transient in both seasons (Figure 3a,b), consistent with N14 and expectation
395 (Thompson and Wallace 2000). The barotropic nature of the propagating regime stands out,
396 where almost the entire peak around lag day -1 comes from m_A and m_{bt} for both EOFs. The
397 positive m_A should be understood as a decrease in wave activity poleward of the jet and
398 increase in wave activity equatorward of it during the poleward phase of SAM, and vice versa
399 for equatorward SAM. This is consistent with the inverse relationship between FAWA and
400 zonal wind (Wang and Nakamura 2015; Nakamura and Huang 2018). However, as discussed
401 in section 2, where m_A is large, m_{up} may be driving m_A rather than the other way around,
402 suggesting caution when interpreting the budget during SAM's generation. Despite this,
403 given good agreement with previous work and theoretical expectation (N14, Thompson and
404 Wallace 2000), interpreting the EMFC as predominantly barotropic and transient seems
405 reasonable. Given the strong negative correlation between wave activity and zonal velocity,
406 we also interpret the pulsing variability (EOF2) in Figure 3e,f as primarily transient during its
407 generation (short negative lags).

408 Interestingly, diabatic heating is adding pseudomomentum in phase with SAM during
409 its generation, particularly during DJF. This could be evidence of a diabatic reinforcement of
410 SAM by damping wave activity equatorward of the jet and generating it poleward of the jet
411 during equatorward SAM, "boosting" the barotropic dynamics responsible for SAM and akin
412 to baroclinic injection of momentum. We reiterate that this diabatic reinforcement is only the
413 eddy effect of diabatic heating; lower-level adjustments to baroclinicity by diabatic heating
414 are not considered to be direct effects of diabatic heating and are not quantified here. Thus, it
415 should not be assumed that diabatic reinforcement of SAM in MERRA2 implies that the
416 annular mode should be weaker in models without such heating.



417

418 Fig. 3. Partitioning of the upper-level (500-100hPa) vertically-integrated eddy momentum
 419 flux convergence (EMFC) as a function of lag in 6-hourly MERRA2 data for 2005-2019
 420 using the wave activity budget [Eq. (9)]. SAM pseudomomentum sources are analyzed

17

421 separately for DJF (a) and MAMJJASON (b) in EOF1 and DJF (e) and MAMJJASON (f) in
422 EOF2. SAM feedbacks, calculated following N14 (see Section 3a), are also shown separately
423 as a function of lag for EOF1 DJF (c) and MAMJJASON (d) and EOF2 DJF (g) and
424 MAMJJASON (h). m_{up} is the upper-level EMFC projected onto the SAM, m_A are the
425 changes in wave activity (pseudomomentum), which contribute to and respond to m_{up}
426 (section 2), m_{bt} is the “barotropic” component of m_{up} driven by irreversible potential
427 vorticity mixing, m_{bc} is the “baroclinic” component of m_{up} from the eddy heat flux
428 convergence [the vertical component of the Eliassen-Palm flux divergence], m_{db} is the
429 “diabatic” component of m_{up} driven by latent and radiative heating, m_{ag} are the ageostrophic
430 contributions to m_{up} , and $\sum m = m_A + m_{bt} + m_{bc} + m_{db} + m_{ag}$ is the reconstruction of
431 m_{up} , which is frequently indistinguishable from m_{up} . Lines appear thin where the
432 bootstrapped 90% confidence interval contains zero.

433

434 At positive lags, both seasons suggest an eddy-jet feedback, evinced by positive
435 correlations of the EMFC with the SAM at lag days 8-12 (Figure 3a,b; Lorenz and Hartmann
436 2001; Simpson et al. 2013) and computed explicitly in Figure 3c,d. The feedback in DJF is
437 larger than in MAMJJASON, which could be attributed to stratospheric influence (Byrne et
438 al. 2016; Saggioro and Shepherd 2019). Another (and not mutually exclusive) possibility is
439 that stationary EOFs have longer EOF1 timescales; faster propagation in MAMJJASON
440 could be reducing the persistence (Lubis and Hassanzadeh 2020).

441 Regardless of the distal cause, the SAM eddy-jet feedback in MERRA2 is
442 proximately due to diabatic heating and the eddy heat flux (Figure 3c,d). For the stationary
443 regime, the diabatic term is the largest positive contributor to the budget for lag days 0-20
444 (Figure 3a). For the propagating regime, the baroclinic term is the largest positive contributor
445 for lag days 2-4, but it has parity with the diabatic term for lag days 5-15 (Figure 3b). EOF2
446 has similar relationships, where the diabatic term is the largest positive term for most lags
447 shown here for the stationary regime, and on par with the baroclinic term for days 0-10 for
448 the propagating regime. Because m_A is statistically indistinguishable from zero during most
449 of this feedback period, we have some confidence here that pseudomomentum injected by
450 diabatic heating is contributing to the positive feedback during this period (Figure 3a,b,d,e).

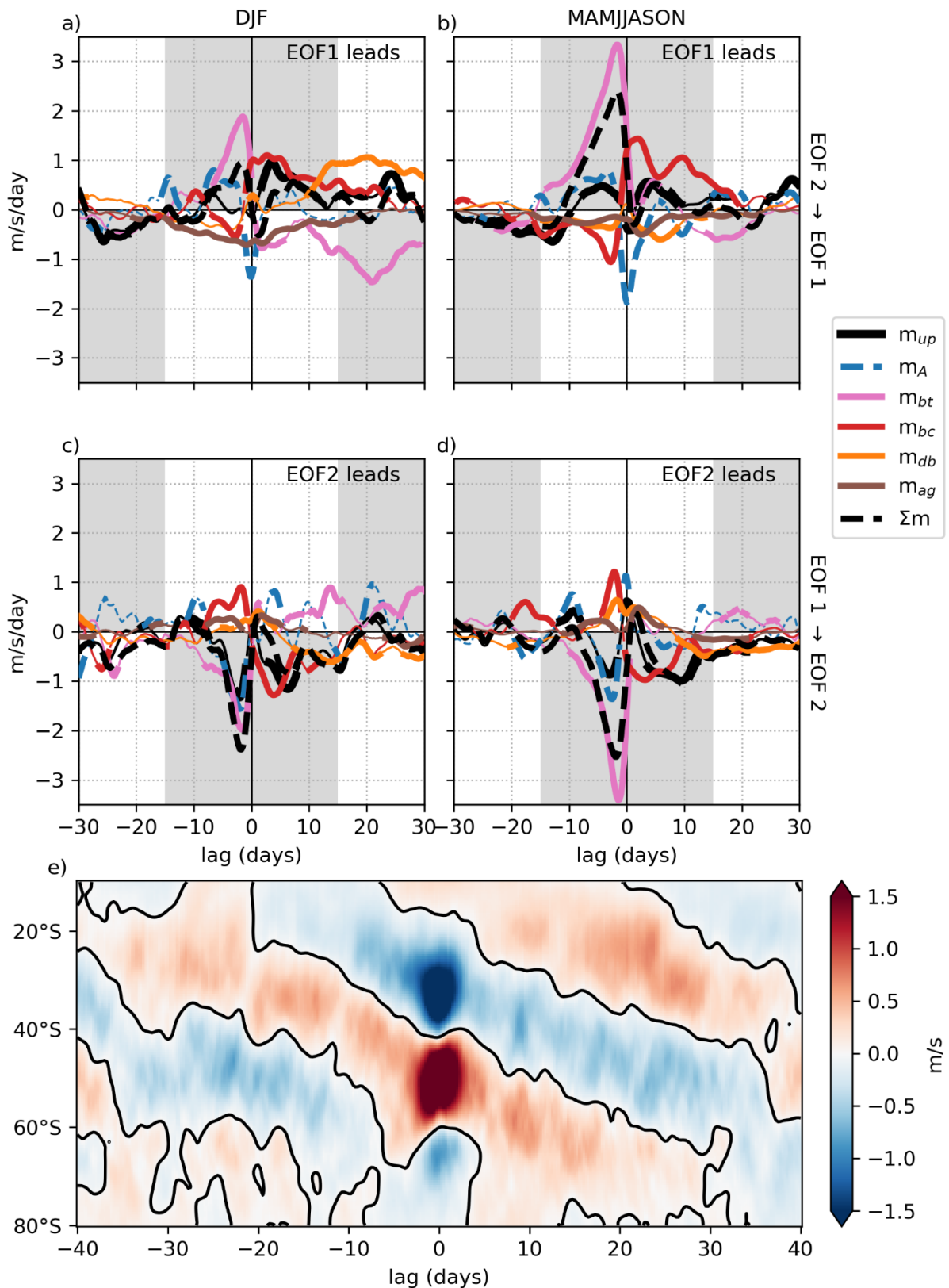
451 A consequence of the importance of diabatic heating is the overestimation of
452 barotropic effects by N14, who implicitly combine the two (c.f. Supplemental Figure 2).
453 Figure 3c,d,g,h shows barotropic mixing is a negative feedback on both EOFs in all seasons,
454 suggesting that wave-breaking is acting to return the jet towards its climatological-mean. N14
455 also neglect ageostrophic effects, but quantifying them reveals their magnitude is about half

456 of the EMFC's at lag days 8-12 for EOF1 (Figure 3a,b). This implies contributions to
457 persistence from ageostrophic eddy fluxes, whose divergence can generate ageostrophic
458 meridional circulations capable of reinforcing SAM-induced baroclinicity anomalies (Nie et
459 al. 2013). Ageostrophic mean meridional circulations have been identified as contributing to
460 persistence in idealized models (Son and Lee 2006; Zurita-Gotor et al. 2014), but deeper
461 investigation of how ageostrophic fluxes might be interacting with SAM in MERRA2 is left
462 to future work.

463 To interpret the cross-EOF pseudomomentum budget, we must determine the period
464 of propagation and choose the (arbitrary) signs for the EOFs. Here, we choose signs such that
465 progression from positive EOF1 to positive EOF2 to negative EOF1 to negative EOF2
466 represents poleward propagation. The period is about 60 days, determined by compositing the
467 propagation events detected using the scheme outlined in section 3a, whose results are shown
468 in Figure 4e. The 60-day period suggested by the compositing analysis is supported by a
469 strong peak in the EOF1 power spectrum at around 60 days (not shown), and it is consistent
470 with earlier, observationally based estimates of meridional propagation (Riehl et al. 1950;
471 Feldstein 1998). Thus, where an EOF2 pseudomomentum source is positively correlated with
472 EOF1 within 15 days of EOF1's peak, that pseudomomentum source is contributing to
473 poleward propagation, and similarly but oppositely for EOF1 pseudomomentum sources.
474 Likewise, the same holds true for negative EOF2 correlations with EOF1 more than 15 days
475 prior to the peak or 15 days after the peak, and vice versa. All of this is captured by the grey
476 shaded regions in Figure 4a-d. Note that the EMFC (black lines in Figure 4) is roughly
477 consistent with poleward propagation at all lags in both seasons, and m_A is generally
478 statistically insignificant/zero outside lag days -5 to 5. Thus, we expect our analysis to pertain
479 reasonably well to changes in zonal momentum, and not just pseudomomentum alone.

480 From the budget for cross-EOF interaction, the barotropic term clearly initiates the
481 poleward propagation (pink lines in Figure 4a-d). This is consistent with the wave-breaking
482 propagation mechanism of Lee et al. (2007) found in an idealized dry model, but, to the best
483 of the authors' knowledge, it has not been confirmed in reanalysis until this work. Consistent
484 with our interpretation of MAMJJASON as the propagating season, the barotropic driver in
485 the propagating regime is nearly twice as strong as it is during DJF. However, it is clear there
486 is still some propagation during DJF, despite it being weaker. The composite analysis

487 confirms the presence of propagation in DJF with 18 of the 81 middle times being in austral
 488 summer.



489

490 Fig. 4. Panels (a-d): As in Figure 3, but for the EOF2 EMFC partitioning regressed against
491 EOF1 (top) and the EOF1 partitioning regressed onto EOF2 (bottom) for DJF (left) and
492 MAMJJASON (right). Grey shaded regions denote signals of poleward propagation of
493 anomalies (positive EOF1 followed by positive EOF2, followed by negative EOF1, and
494 finally negative EOF2), while white regions denote tendencies toward equatorward
495 propagation. Panel (e) shows a composite of zonal-mean zonal angular momentum anomalies
496 during 81 propagation events identified using the method outlined in section 3a from
497 MERRA2 during 2005-2019.

498

499 As previously alluded to, one caveat to this barotropic driving is that the peak day of -
500 2 has a small but significant m_A . Despite this, the agreement with previous findings on the
501 barotropic nature of propagation in idealized models (Lee et al. 2007; Lorenz 2023) suggests
502 that our interpretation is reasonable. Further, m_{bt} is much larger than m_A , and of the same
503 sign, meaning that any changes in pseudomomentum because of barotropic processes are
504 likely not enough to prevent these processes from also impacting zonal momentum.

505 Another caveat with the cross-EOF budget is that our approximation of QG PV as
506 based on the full vorticity (not geostrophic vorticity) is breaking down (see Section 3a). This
507 breakdown is evidenced by the black dashed line [sum of all terms on the rhs of Eq. (8)] not
508 matching the solid black line [lhs of Eq. (8)]. Because m_{bt} is computed residually from Eq.
509 (4), but the sum of all terms relies on Eq. (6), the lack of closure must be due to the
510 connection between the PV flux and the EP flux divergence, which hinges on our
511 computation of PV. This suggests that we may be slightly over-estimating the barotropic
512 term, but not enough to change our conclusions.

513 While the propagation is initiated barotropically, it is sustained baroclinically (red
514 lines in Figure 4). After the barotropic peak in every season and EOF, the baroclinic term
515 becomes the dominant poleward forcing between lag days 1-10. Further, where the eddy heat
516 flux (baroclinic term) is large, the wave activity tendency is generally zero, suggesting that
517 there is baroclinic injection of momentum as a response to the initial anomalies in wave
518 breaking. During the baroclinic response, the barotropic term switches sign, damping the
519 baroclinic response and setting the stage for the next phase of propagation by day 15.

520 If propagation is initiated barotropically and sustained baroclinically, it is primarily
521 opposed by diabatic heating. Diabatic heating from one EOF is generally the same sign as the
522 prior barotropic and baroclinic peaks, but it peaks after both (day 15-20, orange lines in
523 Figure 4). Thus, diabatic pseudomomentum forcing appears in quadrature with the EMFC
524 anomalies, increasing persistence rather than furthering propagation, consistent with the

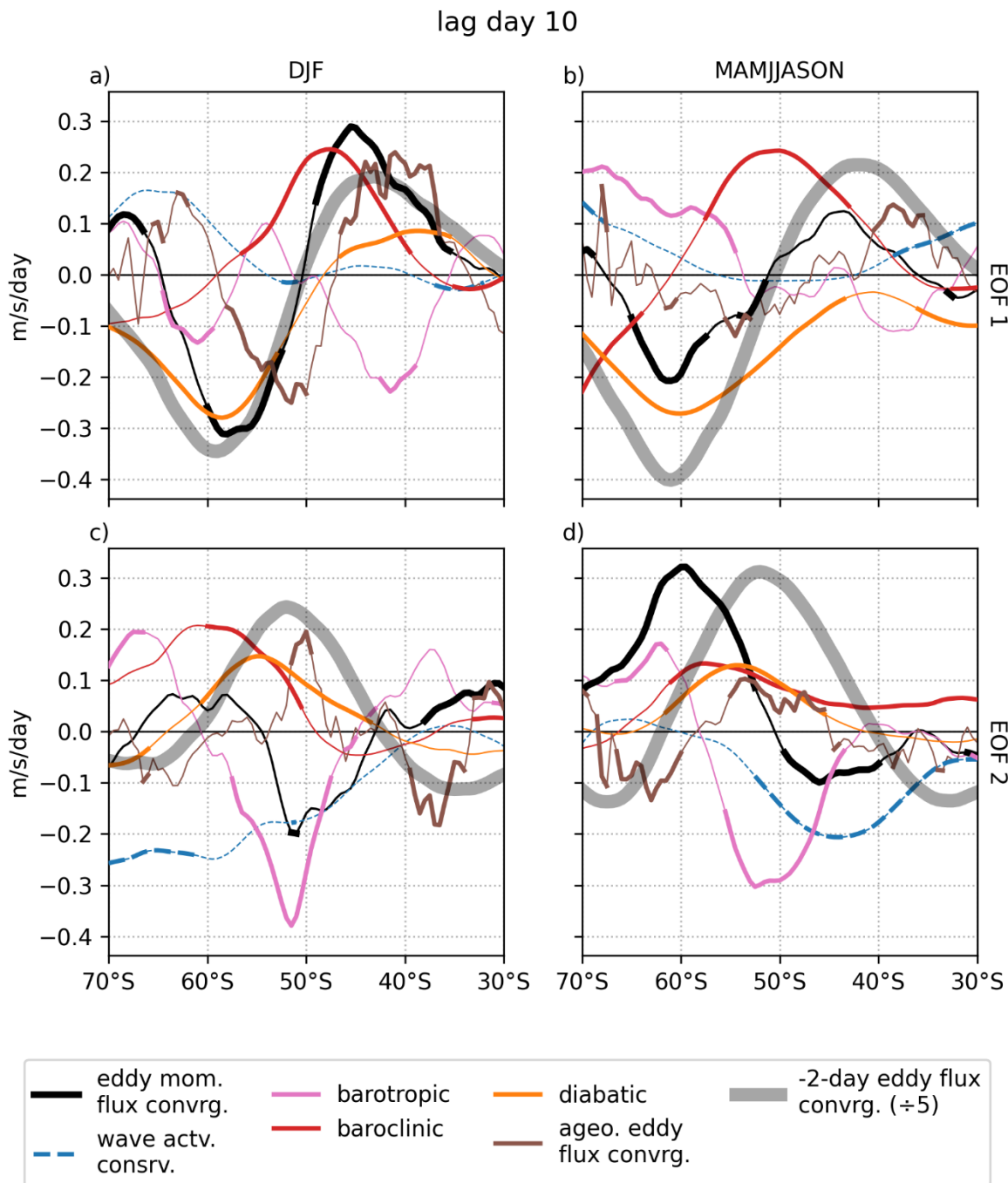
separate EOF budgets (Figure 3). Interestingly, most of this equatorward forcing from diabatic heating comes from the latent heating (see Supplemental Figure 4). This diabatic drag on propagation is strongest in the stationary regime where propagation is weakest (Figure 4a), where the diabatic feedback on EOFs 1 and 2 is also strongest (Figure 3a,c). Ageostrophic momentum also appears to oppose propagation (brown lines in Figure 4) and increase persistence (Figure 3), suggesting that the slower response of both processes to EOF anomalies may favor slower propagation and enhanced persistence.

Diabatic opposition to propagation is consistent with a recently performed series of cloud-locking experiments designed to evaluate the role of CRE for the SAM (Lu et al., 2023). In these atmosphere-only GCM experiments, disrupting CRE-circulation feedbacks increases the robustness of propagation and makes the SAM less persistent, supporting the overall interpretations of the pseudomomentum budgets analyzed here in reanalysis. Overall, we have some confidence that the mechanisms depicted in idealized and realistic modelling studies are realized in reanalysis as well - a barotropic initiation of propagation, a baroclinic maintenance, and a diabatic opposition.

To gain more physical insight, we now examine where these pseudomomentum forcings are operating (Figure 5). At a 10-day lag, the DJF EMFC associated with EOF1 (solid black line in Figure 5a) retains an EOF1-like pattern (thick grey line), consistent with an overall positive feedback. Diabatic contributions to the positive feedback are concentrated poleward of the jet, decelerating the zonal wind there during the equatorward phase of SAM (positive EOF1) through anomalous pseudomomentum absorption (orange line). Baroclinic pseudomomentum generation (red line) is the dominant term equatorward of the jet for EOF1, appearing on the poleward edge of the equatorward EMFC peak, consistent with an enhanced baroclinic injection with an equatorward shift of the storm tracks.

Looking at EOF2, the DJF EMFC has flipped to a negative EOF2 pattern at a 10-day lag, consistent with the absence of both propagation and a positive feedback (Figure 5c). Diabatic FAWA sources are again decelerating zonal wind poleward of the jet. Baroclinic processes (red line) are also concentrated poleward of the jet but further poleward than for EOF1 (Figure 5a). However, these diabatic and baroclinic sources are largely balanced by a growth in wave activity on the poleward jet flank (dashed blue line in Figure 5c), which complicates the interpretation. The negative EOF2 pattern of the EMFC appears to be

556 generated most strongly by the barotropic piece, which is the main negative feedback (Figure
 557 3c).



558

559 Fig. 5. The EMFC partitioning depicted in Figure 3, now latitudinally varying by regressing
 560 onto EOF1 for (a) DJF and (b) MAMJJASON and onto EOF2 for (c) DJF and (d)
 561 MAMJJASON at a 10-day lag. For reference, the thick grey line shows the peak EMFC at
 562 peak day (-2), reduced in magnitude by one-fifth. As before, lines appear thin where the
 563 bootstrapped 90% confidence interval contains zero.

564

565 For the propagating regime at a 10-day lag, we see evidence of propagation in the
566 EMFC, as expected, with diabatic and baroclinic processes contributing in similar regions as
567 in the stationary regime (Figure 5b,d). The baroclinic term is shifted slightly further poleward
568 for EOF1 than in DJF, resulting in a positive EOF2-like pattern (Figure 5b). This shifting of
569 the baroclinic term, combined with more negative diabatic contributions equatorward of the
570 jet, results in an overall weaker positive EOF1 pattern for the EMFC (black line) and thus a
571 weaker feedback than for DJF. Poleward of the jet, the diabatic term is balanced by the more
572 positive barotropic term. The barotropic term has a negative EOF1-like response on the
573 poleward edge of the positive EOF2-like baroclinic response, consistent with the
574 barotropically initiated – baroclinically sustained pattern for propagation.

575 The EOF2 EMFC during MAMJJASON (Figure 5d) shows a clear negative EOF1
576 pattern (c.f. gray shading in Figure 5b) at a 10-day lag, evidence of poleward propagation.
577 Despite this, the diabatic, barotropic, and baroclinic terms largely resemble the stationary
578 regime. Diabatic and baroclinic sources are again primarily contributing poleward of the jet,
579 and the barotropic term is a negative EOF2-like response, in quadrature with the EMFC and
580 consistent with its initiation of propagation. Because there is no statistically significant
581 response in wave activity in this region, we contend that this baroclinic and diabatic injection
582 of momentum poleward of the jet is generating the negative EOF1 pattern which sustains
583 propagation. This highlights the careful synchronization between diabatic heating, upper-
584 level wave growth, and lower-level eddy-heat flux required for propagation (Lee et al. 2007).
585 Diabatic contributions are further examined in section 4b.

586 *4b. SAM Diabatic Pseudomomentum Sources*

587 As discussed in section 2, diabatic pseudomomentum is the sum of pseudomomentum
588 from several heating sources. We now separately consider diabatic contributions from latent
589 heating, long- and short-wave clear-sky radiative heating, and long- and short-wave cloud
590 radiative heating. Shortwave contributions (shown in Supplemental Figure 3) are found to be
591 generally opposing longwave contributions, but they are an order of magnitude smaller. Thus,
592 while included in the total contributions, we neglect them for the remainder of this analysis.

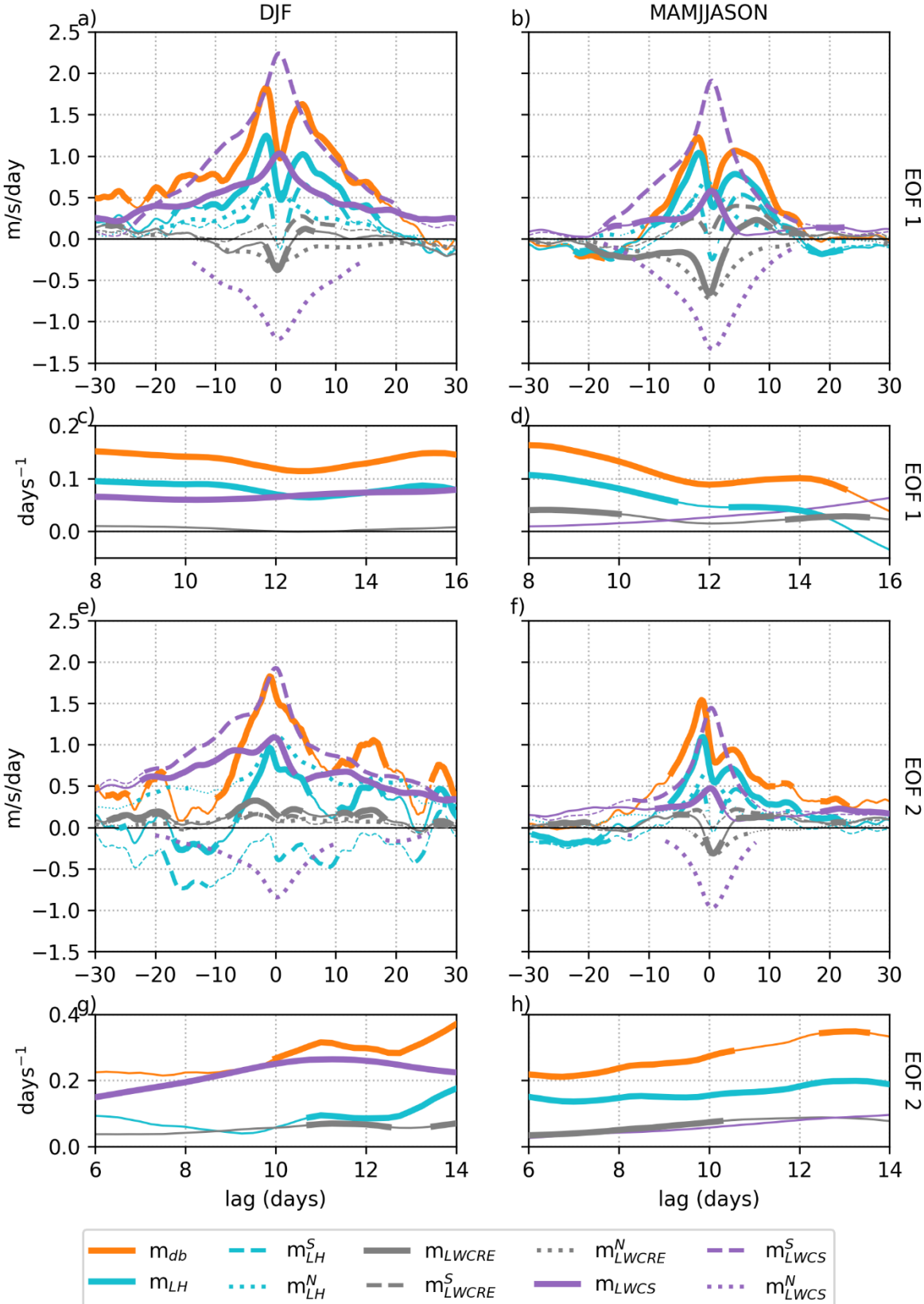
593 The resulting decomposition reveals different processes dominate at different
594 timescales (Figure 6). On short timescales less than ± 10 days, latent heating is generally the
595 largest positive contributor to SAM among the diabatic terms (solid teal lines in Figure 6),
596 except for EOF2 during DJF. In general, much of the temporal structure of the diabatic

597 pseudomomentum forcing comes from the latent heating. Consistent with Lutsko and Hell
598 (2021), we find latent heating is a positive feedback on SAM persistence (Figure 6c,d,h).
599 While this may seem at odds with Xia and Chang (2014), who argue for a negative latent
600 heating feedback, this eddy-interaction framework does not consider indirect diabatic
601 contributions from the adjustment of low-level baroclinicity, which are instead included in
602 the baroclinic term by attenuating the heat flux from the lower troposphere into the upper
603 troposphere.

604 While the role of latent heating is generally consistent across regimes, clear-sky
605 pseudomomentum contributions primarily explain the difference between stationary and
606 propagating regimes (solid purple lines in Figure 6). The clear-sky forcing is exclusively
607 positive, with a magnitude ranging from 2-5 times larger during DJF than during
608 MAMJJASON (Figure 6). Because clear-sky contributions are the dominant diabatic
609 contributions beyond lag day 10 in DJF (Figure 6a), and because diabatic terms are the
610 largest positive contributions for the entire budget (Figure 3a), clear-sky heating explains
611 much of the increased persistence of the stationary regime (Figure 6c,h vs Figure 6d,g).

612 While clear-sky and latent heating dominate at their respective timescales, cloud
613 radiative heating is a second-order contributor to SAM dynamics (solid grey lines in Figure
614 6). Given the relatively weak cloud response and complex vertical structure of the cloud
615 heating (Li and Thompson, 2016), this is unsurprising. However, despite being a small
616 pseudomomentum source, it is the only term to clearly change sign over time in EOF1. At
617 leads -10 to around lag day 2, cloud contributions are negative, but after lag day 3, the cloud
618 contributions are positive, peaking around lag days 5-8 and weakly increasing SAM
619 persistence (Figure 6b,d). This may partially explain the challenge in diagnosing cloud
620 impacts.

621 Further breaking the pseudomomentum into separate contributions from cyclonic and
622 anticyclonic waves, nearly all the positive forcing comes from anticyclonic waves (dashed
623 lines in Figure 6). Radiative heating within cyclonic waves opposes SAM in all seasons for
624 all EOFs (dotted purple and grey lines). For clear-sky heating, the total contributions result
625 from a large compensation between anticyclonic contributions, peaking between 1.5-2
626 m/s/day, and cyclonic contributions, peaking between 1-1.5 m/s/day. One explanation for this
627 result may be that radiative heating is strengthening both cyclonic waves on one flank of the
628 jet and anticyclonic waves on the opposite flank, resulting in competing effects.



629

630 Fig. 6. As in Figure 3, but the upper-level pseudomomentum contributions of different
 631 diabatic processes [Eq. (10)]. m_{db} is the same diabatic component of m_{up} as in Figure 3,
 632 calculated as the sum of the following terms: m_{LH} is the component of m_{up} driven by latent

heat release, $m_{\text{LWC}\text{RE}}$ is the component of m_{up} driven by longwave (LW) cloud radiative heating (all-sky minus clear-sky), and $m_{\text{LW}\text{CS}}$ is the component of m_{up} driven by LW clear-sky radiative heating. Shortwave cloud and clear-sky cooling are included in m_{db} , but they are left for Supplemental Figure 3 as they are negligible. Also shown separately are contributions from anticyclonic (southward) wave breaking (superscript S) and cyclonic (northward) wave breaking (superscript N).

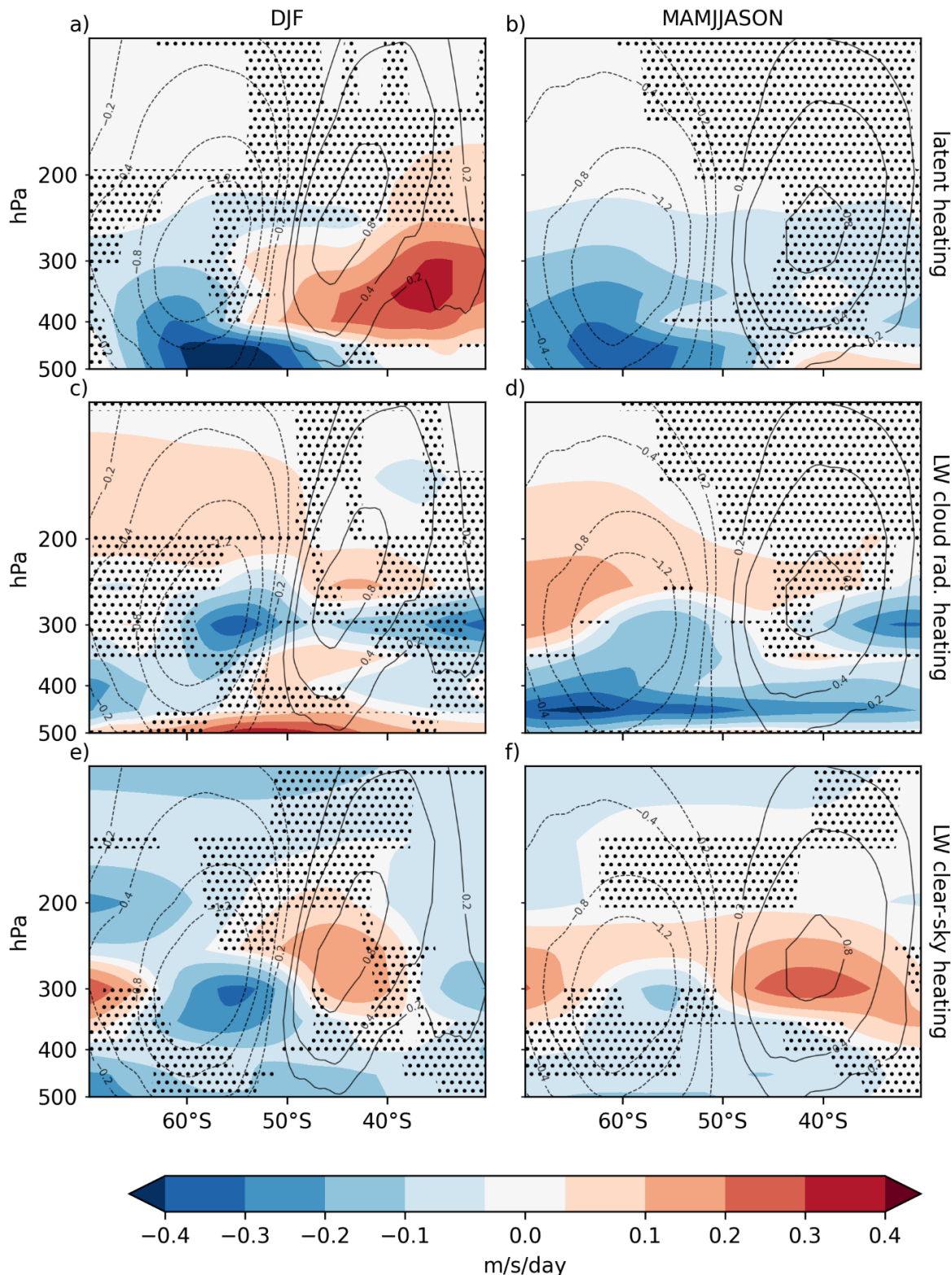
639

To test this hypothesis and gain more insight into how diabatic heating modulates wave activity and momentum, we again analyze the response's spatial pattern. Adding the vertical dimension, we see that diabatic pseudomomentum for EOF1 is not only concentrated poleward of the jet, but also below 300hPa (Figure 7). For the stationary regime, latent heating broadly reinforces the peak-day EMFC anomaly (contour lines), in-phase with the anomaly on both flanks of the jet and still at nearly half of the magnitude of the peak EMFC ten days later (Figure 7a). This is likely from an equatorward shift of the storm tracks, as we show in section 4c. During the propagating regime, latent heating is also in-phase around 500hPa poleward of the jet, somewhat weaker than during the stationary regime (Figure 7b).

The radiative contributions from cloud and clear-sky heating are less in-phase with the EMFC anomalies than latent heating, and they are mostly concentrated below 200hPa. Cloud radiative heating is weakly in-phase with EMFC anomalies poleward of the jet for both seasons (Figure 7c,d). Cloud contributions have the most vertical variation of the diabatic terms, which is significant because the net impact results from a vertical average. Because there is great uncertainty in SAM's influence of the vertical profile of cloud heating (Li and Thompson, 2016), their small magnitude identified in MERRA2 may not be reproduced by other reanalyses or models.

Clear-sky pseudomomentum sources exhibit the most variation of all the diabatic sources for EOF1 (Figure 7e,f). Clear-sky forcing during the stationary regime is well-aligned with the EMFC anomalies, acting to decelerate the zonal wind poleward of the jet throughout the entire upper troposphere (since $m_A \approx 0$ at lag day 10; Figure 7e). In contrast, the propagating regime exhibits approximately 50% weaker clear-sky influence and is generally less in-phase with the EMFC poleward of 50°S (Figure 7f). This result could support proposals for a stratospheric influence on EOF1 during DJF (Byrne et al. 2016, Saggioro and Shepherd 2019), if stratospheric temperature anomalies are modifying upper-tropospheric longwave radiation. Further investigation for a radiative pathway for stratospheric influence is left for future work.

EOF 1, 10-day lag



667

668 Fig. 7. The diabatic contributions to SAM pseudomomentum depicted in Figure 6, regressed
 669 onto the EOF1 index at a 10-day lag (shading). Contributions are shown from (a,b) latent
 670 heating (m_{LH}), (c,d) cloud longwave heating (m_{LWCRE}), and clear-sky longwave heating

28

671 (m_{LWCS}) for DJF and MAMJJASON, respectively. Contours are the eddy momentum flux
672 convergence at day zero (in m/s/day) for reference. Stippling represents regions where
673 bootstrapped 90% confidence intervals contain zero.

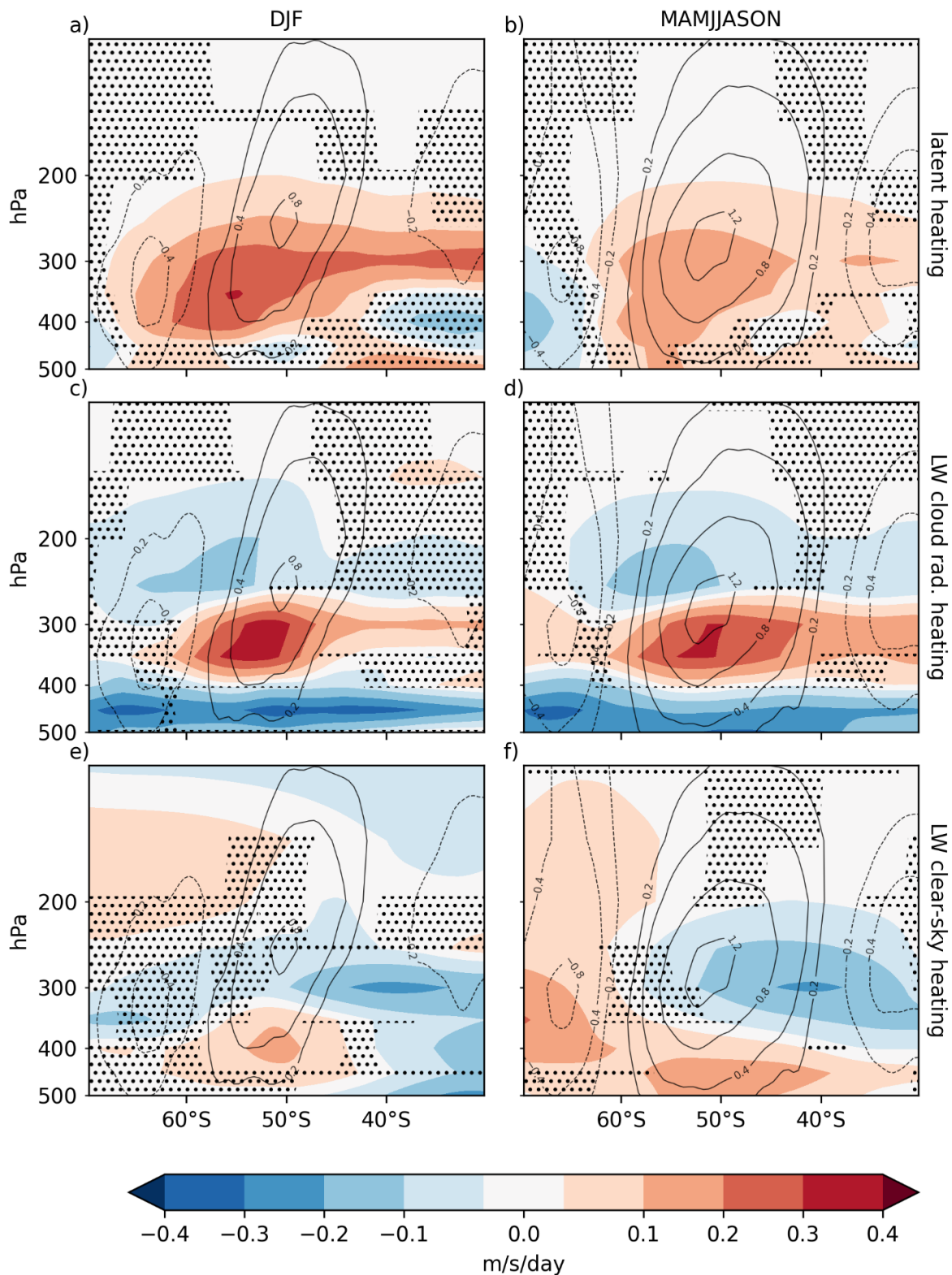
674

675 When looking at the spatial structure of diabatic pseudomomentum for EOF2, we see mostly
676 reinforcement of the EOF2 EMFC pattern at a 10-day lag (Figure 8). This is particularly the
677 case for latent and cloud radiative heating, which reinforce the stronger jet in the mid-
678 troposphere in all seasons (Figure 8a-d). In both seasons, the cloud contributions to EOF2
679 (Figure 8c,d) are mostly opposite sign to their EOF1 contributions (Figure 7c,d), still
680 exhibiting the most cancellation in the vertical mean. Clear-sky heating projects weakly onto
681 EOF2, largely within -0.1 to 0.1 m/s/day. During the propagating regime, clear-sky
682 contributions (Figure 8f) are a weak negative EOF1-like pattern (cf. Figure 7f), but this is
683 unlikely to be supporting propagation considering the previous analysis. In section 4c, we
684 analyze wave-breaking regions to identify physical mechanisms for the diabatic feedbacks
685 and to investigate the role of anticyclonic and cyclonic circulation interactions.

686 *4c. Analysis of large breaking waves*

687 The final part of this analysis identifies regions of large, nonlinear, upper-level
688 cyclonic and anticyclonic waves to detect consistent trends between physical drivers of
689 diabatic heating and its impact on pseudomomentum. This reveals probable mechanisms
690 through which changes in jet latitude (the EOF1 mode) might lead to the diabatic feedbacks
691 described in the previous section. We focus on regions of large wave activity because they
692 should have an outsized impact on the wave activity budget and thus on zonal momentum,
693 and because we expect the underlying dynamics of the largest waves to be similar. A separate
694 analysis on these large wave events reveals that over 90% of the waves exhibit overturned PV
695 contours (see random subsample in Supplemental Figures 5 and 6), in agreement with the
696 theoretical expectation that waves in the early stages of breaking should be the largest
697 contributors to wave activity (Nakamura and Huang 2017). Wave-breaking is also known to
698 play an important role in the lifecycle of SAM's generation and feedbacks (Thompson and
699 Wallace 2000, Barnes et al. 2010), thus, our analysis of the large cyclonic breaking waves
700 (CBW) and anticyclonic breaking waves (ABW) should provide insight into how diabatic
701 heating can interact with waves to influence SAM's dynamics.

EOF 2, 10-day lag



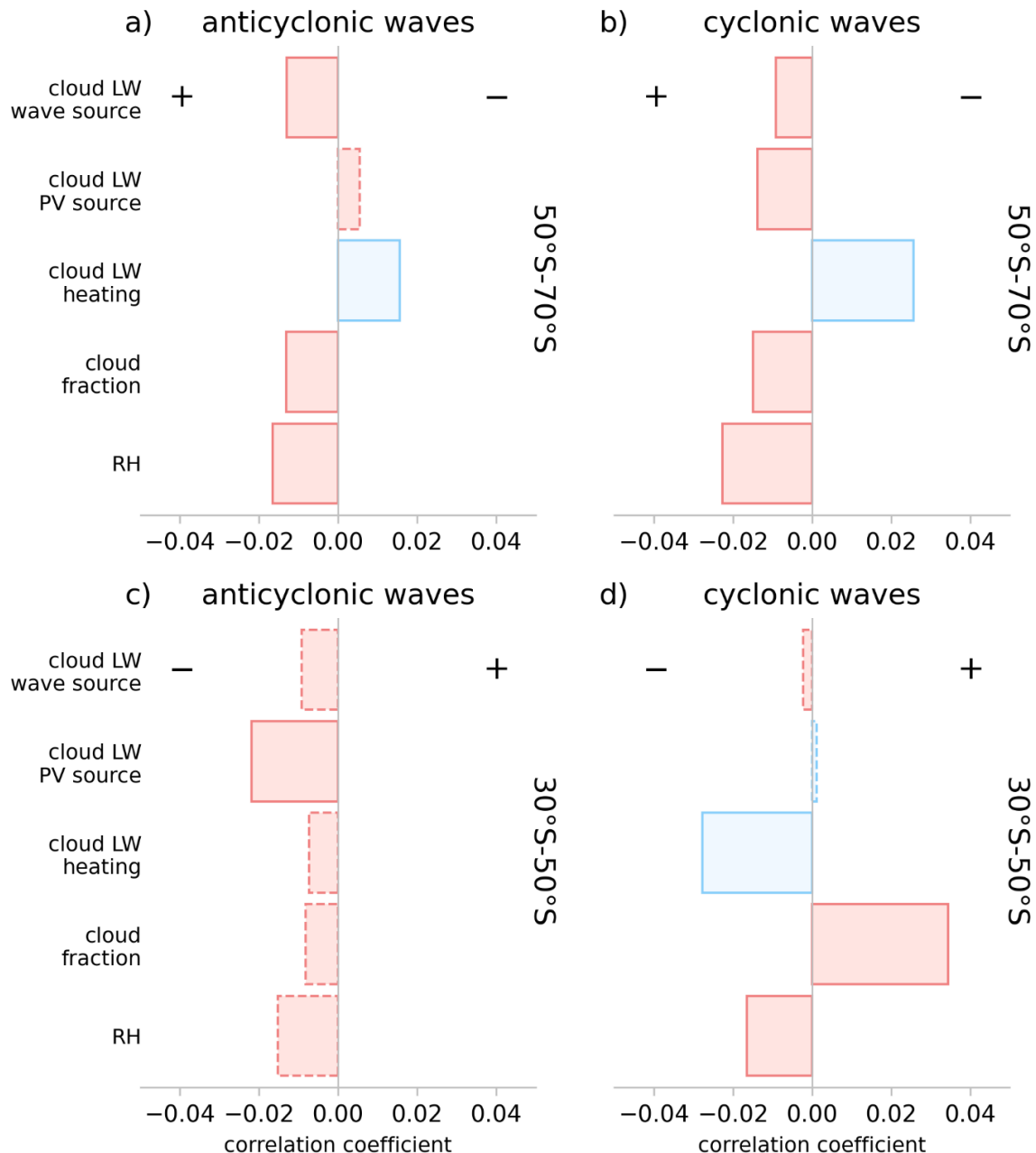
704 Fig. 8. As in Figure 7, but regressed against the EOF2 index.

We examine correlations between EOF1 and large breaking waves at a 10-day lag, both poleward of the jet (50° - 70° S) and equatorward of the jet (30° - 50° S). We make this distinction for two reasons. First and foremost, the EMFC has different signs on opposite sides of the jet (approximately 50° S), and so a positive diabatic wave forcing may reinforce or oppose this pattern depending on its latitude (as suggested by the plus/minus signs in Figures 9-11). Second, the distributions of these fields are quasi-bimodal, and they are more Gaussian if first separated by latitude (not shown). Since we might reasonably expect similar diabatic responses to EOF1 regardless of the season, we focus our efforts on year-round data to help improve the signal against the noisiness of synoptic-scale weather systems.

Consistent with previous regressions (Figure 7d), the positive longwave (LW) cloud feedback seen in Figure 6b is primarily coming from decreases in the cloud pseudomomentum source in both poleward ABW (PABW) regions and poleward CBW (PCBW) regions (Figure 9a,b). Note the signs for pseudomomentum sources follow the convention described in section 2. This decreased wave source is accompanied by a consistent weakening of upper-level cloud LW cooling in both regions, along with decreases in upper-level relative humidity and cloud fraction. Physically, this suggests this diabatic feedback may be due to a reduced cloud fraction resulting from an upper-level reduction in relative humidity in response to the more equatorward jet.

The effects of heating on PV depend on the vertical profile of the heating (c.f. Eq. (5)), and so changes (or lack thereof) in the vertically-averaged heating do not directly imply changes in PV. Even so, there is a reduction of the cloud cyclonic PV generation for PCBW (Figure 9b) and a weak increase in the cloud anticyclonic PV source for PABW (Figure 9a), which we might expect given that cloud LW cooling weakens similarly in both regions.

Looking at equatorward ABW (EABW), there are few significant relationships between SAM and these cloud-related variables (Figure 9c). There are no significant changes to the dynamical measures in equatorward CBW (ECBW) regions as well, though we do see a robust increase in cloud LW cooling coincident with increased cloud fraction, opposite the response in poleward regions (Figure 9d). Given the negative cloud pseudomomentum anomalies between 30° - 50° S in Figure 7d, it is likely there is a weak negative feedback in the equatorward regions that is difficult to identify amidst the noise. However, the wave activity budget (Figure 6b) shows this negative feedback in equatorward regions is weaker than the positive one in poleward regions.



737

738 Fig. 9. Correlation coefficients of EOF1 with the 10-day-lagged, 500-100hPa-averaged, year-
739 round relative humidity, cloud fraction, longwave cloud heating, the longwave cloud heating
740 PV source, and the longwave cloud contribution to wave activity for a) anticyclonic wave
741 regions, between 50-70 degrees south, b) cyclonic wave regions, between 50-70 degrees
742 south, c) anticyclonic wave regions, between 30-50 degrees south, and d) cyclonic wave
743 regions, between 30-50 degrees south. Blue shading indicates that the mean value of the field
744 for each composite region is negative; red shading indicates the mean value is positive. Signs
745 are chosen for the PV source and wave activity source fields to match the sign of the PV
746 anomaly, i.e. a positively correlated PV source for anticyclonic waves corresponds to
747 anticyclonic strengthening, whereas a positively correlated source for cyclonic waves
748 corresponds to cyclonic strengthening. Plus/minus signs by the wave activity source
749 correlations indicate whether the changes are same-signed (+) or opposite-signed (-) as the

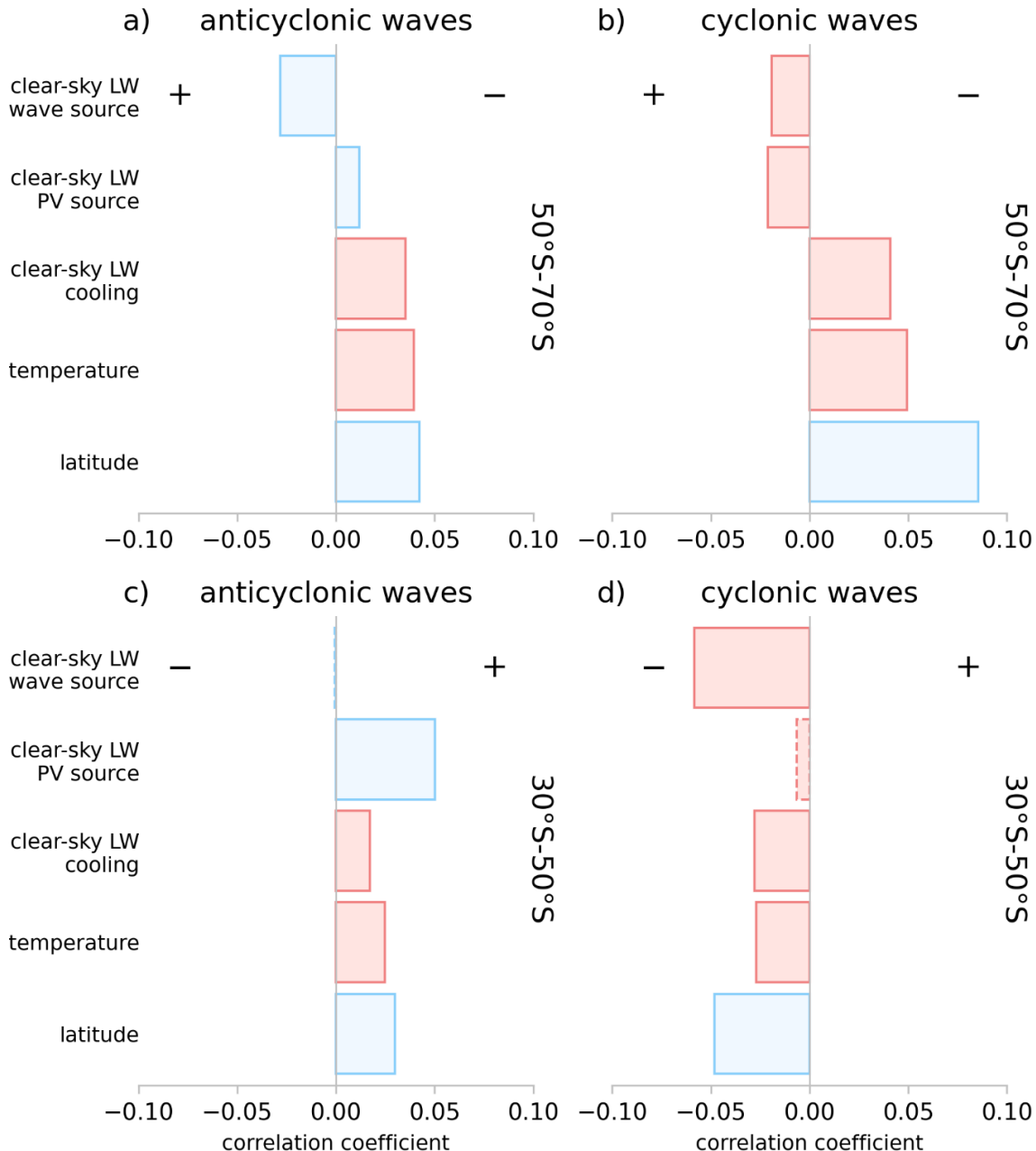
750 SAM momentum anomalies (i.e., either a positive or a negative feedback). Dashed outlines
751 are not significant correlations at the 95% confidence level.

752

753 Changes in pseudomomentum from clear-sky heating are similarly positive in
754 poleward regions, where an equatorward jet is linked to more equatorward and thus warmer
755 waves for PABW, PCBW, and EABW regions (Figure 10a-c). The warmer temperatures
756 coincide with increased longwave cooling in all these regions as well as increased
757 anticyclonic PV generation or cyclonic PV damping (Figure 10a-c). This suggests the
758 positive clear-sky feedback comes from the equatorward shift of the storm tracks, producing
759 warmer waves with increased longwave cooling in poleward waves, strengthening ABW and
760 weakening CBW.

761 Interestingly, ECBW shows opposite trends to the other regions (Figure 10d). Here,
762 we see a decrease in the pseudomomentum source, implying a negative feedback. This is
763 consistent with a counter-intuitive shift towards higher latitude CBW (during equatorward
764 SAM), a reduction in temperature, and a weakening of clear-sky cooling (Figure 10d).
765 However, our previous results suggest that SAM's clear-sky heating acts as a positive
766 feedback equatorward of the jet (Figures 6b and 7f), so this negative feedback would imply
767 that the lower nine deciles of wave activity provide the positive feedback, countervailing the
768 changes seen in this top decile. Another consideration is the fact that we are tracking
769 equivalent latitudes, and that, somewhat paradoxically, ABW tends to be identified at higher
770 equivalent latitudes than CBW (Supplemental Figure 7).

771 To conclude this analysis, we examine fields relevant to latent heating at a 10-day lag,
772 which also suggest the positive feedback is due to the shift in storm tracks (Figure 11). As
773 with the clear-sky fields, the equatorward shift in cyclones and anticyclones result in more
774 moisture availability and stronger latent heating in PABW, PCBW, and EABW regions
775 (Figure 11a-c). Where the latent heating increase is robust, it strengthens EABW and
776 weakens PCBW, injecting pseudomomentum equatorward of the jet and removing it on the
777 poleward flank, thus acting as a positive feedback. These results are consistent with Figures
778 7b and 6b, as well as with observational studies finding that latent heating increases the
779 persistence of the North Atlantic storm track (Woollings et al. 2016). The most robust
780 changes are seen for PCBW, where cyclones shift more equatorward, and thus have more
781 moisture available for latent heating (Figure 11b).



782

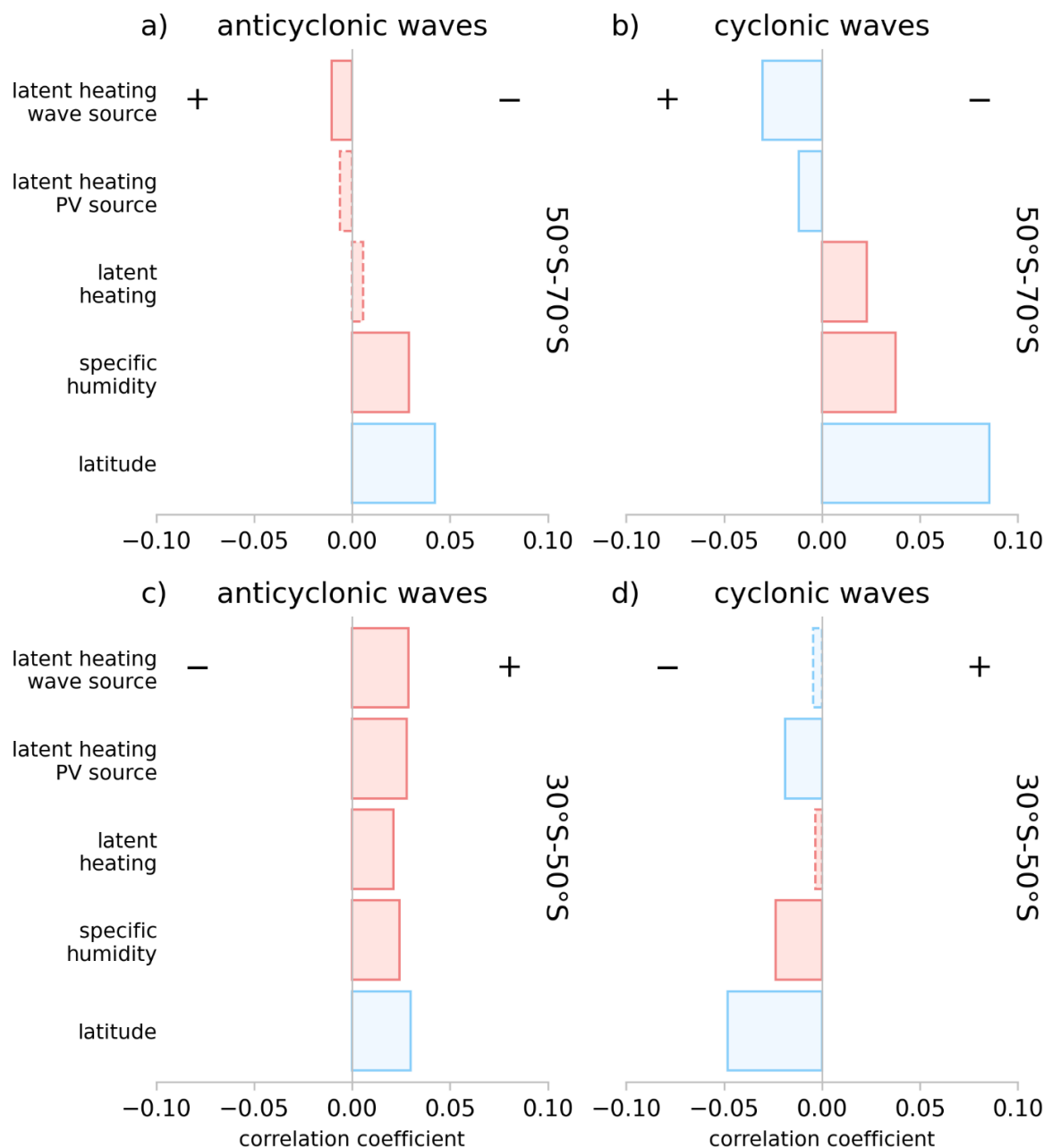
783 Fig. 10. As in Figure 9, but for 500-100 hPa centroid latitude, temperature, longwave clear-
784 sky cooling (negative heating), longwave clear-sky PV source, and longwave clear-sky wave
785 activity contribution. The sign convention for PV sources and wave sources is the same as
786 Figure 9.

787

788 Like the clear-sky response, the pattern is reversed for ECBW regions: more poleward
789 cyclones, with less moisture available and mildly weaker latent heating (Figure 11d). While
790 the changes to CBW equatorward of the jet during SAM are not consistent with the other
791 regions, they are internally consistent, suggesting that this analysis does identify the relevant
792 physical mechanisms which are mediating the diabatic feedbacks on SAM. Thus, 10 days

793 after peak equatorward SAM, storm tracks are still displaced, increasing the latent heating
794 and clear-sky radiative cooling poleward of the jet, weakening upper level waves and
795 enhancing SAM's persistence.

796



797

798 Fig. 11. As in Figure 9, but for 500-100 hPa centroid latitude, specific humidity, latent
799 heating tendency, latent heating potential vorticity source, and latent heating contributions to
800 pseudomomentum.

801

802 **5. Conclusions**

803 To quantify the contributions of diabatic, barotropic, and baroclinic processes to the
804 persistence and propagation of SAM, we have examined a detailed partitioning of the EMFC
805 in MERRA2 from 2005-2019 using the finite-amplitude wave activity framework.
806 Principally, we find that diabatic heating, particularly from latent and longwave clear-sky
807 heating, is the dominant pseudomomentum source at positive lags during DJF, for both the jet
808 shift (EOF1) and jet pulsing (EOF2) modes of variability. Thus, diabatic effects constitute the
809 largest eddy-jet feedback for the stationary regime of SAM variability. This is a novel
810 contribution of this work which corrects the earlier work of N14.

811 Because diabatic heating is the largest feedback during DJF, and because this
812 feedback is tied to the latitude of wave breaking and thus the jet itself, efforts to improve
813 representation of SAM in models should first consider the climatological jet latitude.
814 However, improved climatological jet latitudes have not eliminated DJF timescale biases in
815 CMIP6 (Bracegirdle et al. 2020), and these results urge further consideration of whether the
816 often-parameterized diabatic processes in models generate a realistic vertical profile of
817 heating in response to SAM.

818 We emphasize that the presence of a positive feedback from latent heating in reanalysis
819 does not imply that dry models should have shorter SAM timescales. Because of the tight
820 coupling between the eddy-mean flow interactions which govern the annular mode's
821 evolution, removing one process (such as latent heating) has too many compounding effects
822 to suggest a linear response of SAM's timescale. However, our results do suggest caution
823 when generalizing findings from idealized, dry models commonly utilized to study annular
824 mode dynamics to findings about the real atmosphere.

825 For the propagating regime of SAM variability during March-November, we find
826 baroclinic contributions from the meridional eddy heat flux are the largest pseudomomentum
827 source for EOF1 and EOF2 at positive lags, followed closely by diabatic heating.
828 Additionally, barotropic contributions initiate the EOF1-EOF2 interaction which drives
829 poleward propagation, which is supported by a baroclinic response. Diabatic heating
830 generally opposes poleward propagation, consistent with the finding that it increases
831 persistence (Lubis and Hassanzadeh 2020).

832 Additionally, diabatic heating may explain the tendency towards a stationary regime
833 in DJF through a stronger clear-sky pseudomomentum source and a stronger damping of
834 propagation than in MAMJJASON. More fundamentally, the tendency towards propagation
835 or non-propagation has been explained as result of double or single jet states (Lee et al 2007),
836 the latter being more common in summer due to the weakened eddy-driven jet. These
837 mechanisms are not mutually exclusive – jet latitude has an important influence over diabatic
838 heating. These results for the propagating regime highlight the careful orchestration between
839 processes required to produce an accurate SAM timescale and thus to predict SAM evolution.
840 Future progress relies on identifying the controls on the speed of propagation and partitioning
841 the EMFC in full-physics models.

842 In tandem with this work, some of the authors have partitioned the SAM EMFC in a
843 suite of “cloud-locking” experiments in the Exascale Energy Earth System Model (E3SM)
844 designed to eliminate cloud-circulation feedbacks (Lu et al. 2023). Lu et al. (2023) also
845 utilize the wave activity framework to explain how CRE produces a positive feedback to
846 SAM in E3SM, in part by disrupting propagation in a manner consistent to the findings of
847 this work for MERRA2.

848 A final caveat is suggested by the results of Chemke and Polvani (2019), who argue
849 that discrepancies between reanalyses and models sometimes represent deficiencies in the
850 reanalyses and not the models, as in the case of trends in Hadley cell strength. While this
851 analysis cannot definitively demonstrate the validity of these results beyond MERRA2, this
852 work is internally consistent and broadly in agreement with modeling studies, suggesting that
853 our key findings on the importance of diabatic heating for SAM are likely not a result of
854 artefacts in MERRA2.

855 Our approach taken here elucidates many different facets controlling the variability of
856 the Southern Hemisphere zonal wind. We find diabatic heating is crucial to setting the
857 timescale of a largely barotropic phenomena. We also find consistencies between reanalysis
858 and idealized modeling studies, increasing our confidence that mechanisms operating in the
859 idealized studies are also operating in the real atmosphere. We contend that coupling this
860 budget-based approach with targeted model experiments could be an ideal strategy for
861 determining the underlying controls for a host of annular mode behaviors.

862 *Acknowledgments.*

863 We thank the editor and two anonymous reviewers whose comments have improved
864 this manuscript. We acknowledge NASA for its provision of MERRA2 data. Python libraries
865 Numpy, matplotlib, and xarray expedited the analysis and visualization. This research was
866 partially supported by Lilly Endowment, Inc., through its support for the Indiana University
867 Pervasive Technology Institute. S.S. is supported under NASA FINESST Award
868 80NSSC21K1596, P.S. under NSF Grant 1813981, and J.L. by the DOE Office of Science
869 Biological and Environmental Research as part of the Regional and Global Modeling and
870 Analysis program area.

871 *Data Availability Statement.*

MERRA2 data is publicly available from NASA GES DISC (DOI: 10.5067/A7S6XP56VZWS; 10.5067/9NCR9DDDOPFI). Code for computing the local wave activity budget is available from the corresponding author upon request.

REFERENCES

- 877 Andrews, D. G., 1987: *Middle atmosphere dynamics*. J.R. Holton and C.B. Leovy, Eds.
878 Academic Press.

879 Baldwin, M. P., and T. J. Dunkerton, 2001: Stratospheric Harbingers of Anomalous Weather
880 Regimes. *Science*, **294**, 581–584, <https://doi.org/10.1126/science.1063315>.

881 ——, D. B. Stephenson, and I. T. Jolliffe, 2009: Spatial Weighting and Iterative Projection
882 Methods for EOFs. *Journal of Climate*, **22**, 234–243,
883 <https://doi.org/10.1175/2008JCLI2147.1>.

884 Barnes, E. A., D. L. Hartmann, D. M. W. Frierson, and J. Kidston, 2010: Effect of latitude on
885 the persistence of eddy-driven jets. *Geophysical Research Letters*, **37**,
886 <https://doi.org/10.1029/2010GL043199>.

887 Blanco-Fuentes, J., and P. Zurita-Gotor, 2011: The driving of baroclinic anomalies at
888 different timescales. *Geophysical Research Letters*, **38**,
889 <https://doi.org/10.1029/2011GL049785>.

890 Boljka, L., T. G. Shepherd, and M. Blackburn, 2018: On the Coupling between Barotropic
891 and Baroclinic Modes of Extratropical Atmospheric Variability. *Journal of the*
892 *Atmospheric Sciences*, **75**, 1853–1871, <https://doi.org/10.1175/JAS-D-17-0370.1>.

893 Bracegirdle, T. J., C. R. Holmes, J. S. Hosking, G. J. Marshall, M. Osman, M. Patterson, and
894 T. Rackow, 2020: Improvements in Circumpolar Southern Hemisphere Extratropical

- Atmospheric Circulation in CMIP6 Compared to CMIP5. *Earth and Space Science*, **7**, e2019EA001065, <https://doi.org/10.1029/2019EA001065>.
- Byrne, N. J., T. G. Shepherd, T. Woollings, and R. A. Plumb, 2016: Annular modes and apparent eddy feedbacks in the Southern Hemisphere. *Geophysical Research Letters*, **43**, 3897–3902, <https://doi.org/10.1002/2016GL068851>.
- Chemke, R., and L. M. Polvani, 2019: Opposite tropical circulation trends in climate models and in reanalyses. *Nat. Geosci.*, **12**, 528–532, <https://doi.org/10.1038/s41561-019-0383-x>.
- Feldstein, S. B., 1998: An Observational Study of the Intraseasonal Poleward Propagation of Zonal Mean Flow Anomalies. *Journal of the Atmospheric Sciences*, **55**, 2516–2529, [https://doi.org/10.1175/1520-0469\(1998\)055<2516:AOSOTI>2.0.CO;2](https://doi.org/10.1175/1520-0469(1998)055<2516:AOSOTI>2.0.CO;2).
- Gelaro, R., and Coauthors, 2017: The Modern-Era Retrospective Analysis for Research and Applications, Version 2 (MERRA-2). *J. Climate*, **30**, 5419–5454, <https://doi.org/10.1175/JCLI-D-16-0758.1>.
- Gerber, E. P., L. M. Polvani, and D. Ancukiewicz, 2008: Annular mode time scales in the Intergovernmental Panel on Climate Change Fourth Assessment Report models. *Geophysical Research Letters*, **35**, <https://doi.org/10.1029/2008GL035712>.
- Gritsun, A., and G. Branstator, 2007: Climate Response Using a Three-Dimensional Operator Based on the Fluctuation–Dissipation Theorem. *Journal of the Atmospheric Sciences*, **64**, 2558–2575, <https://doi.org/10.1175/JAS3943.1>.
- Hassanzadeh, P., and Z. Kuang, 2016: The Linear Response Function of an Idealized Atmosphere. Part II: Implications for the Practical Use of the Fluctuation–Dissipation Theorem and the Role of Operator’s Nonnormality. *Journal of the Atmospheric Sciences*, **73**, 3441–3452, <https://doi.org/10.1175/JAS-D-16-0099.1>.
- Huang, C. S. Y., and N. Nakamura, 2016: Local Finite-Amplitude Wave Activity as a Diagnostic of Anomalous Weather Events. *Journal of the Atmospheric Sciences*, **73**, 211–229, <https://doi.org/10.1175/jas-d-15-0194.1>.
- Kidson, J. W., 1988a: Indices of the Southern Hemisphere Zonal Wind. *Journal of Climate*, **1**, 183–194, [https://doi.org/10.1175/1520-0442\(1988\)001<0183:IOTSHZ>2.0.CO;2](https://doi.org/10.1175/1520-0442(1988)001<0183:IOTSHZ>2.0.CO;2).
- , 1988b: Interannual Variations in the Southern Hemisphere Circulation. *Journal of Climate*, **1**, 1177–1198, [https://doi.org/10.1175/1520-0442\(1988\)001<1177:IVITSH>2.0.CO;2](https://doi.org/10.1175/1520-0442(1988)001<1177:IVITSH>2.0.CO;2).

- 927 Kidston, J., and E. P. Gerber, 2010: Intermodel variability of the poleward shift of the austral
928 jet stream in the CMIP3 integrations linked to biases in 20th century climatology.
929 *Geophysical Research Letters*, **37**, <https://doi.org/10.1029/2010GL042873>.
- 930 Lee, S., and S. Feldstein, 1996: Mechanism of Zonal Index Evolution in a Two-Layer Model.
931 *Journal of the Atmospheric Sciences*, **53**, 2232–2246, [https://doi.org/10.1175/1520-0469\(1996\)053<2232:MOZIEI>2.0.CO;2](https://doi.org/10.1175/1520-0469(1996)053<2232:MOZIEI>2.0.CO;2).
- 933 ——, S.-W. Son, K. Grise, and S. B. Feldstein, 2007: A Mechanism for the Poleward
934 Propagation of Zonal Mean Flow Anomalies. *Journal of the Atmospheric Sciences*,
935 **64**, 849–868, <https://doi.org/10.1175/JAS3861.1>.
- 936 Li, Y., and D. W. J. Thompson, 2016: Observed Signatures of the Barotropic and Baroclinic
937 Annular Modes in Cloud Vertical Structure and Cloud Radiative Effects. *Journal of*
938 *Climate*, **29**, 4723–4740, <https://doi.org/10.1175/JCLI-D-15-0692.1>.
- 939 ——, ——, Y. Huang, and M. Zhang, 2014: Observed linkages between the northern annular
940 mode/North Atlantic Oscillation, cloud incidence, and cloud radiative forcing.
941 *Geophysical Research Letters*, **41**, 1681–1688,
942 <https://doi.org/10.1002/2013GL059113>.
- 943 Liu, S., P. W. Staten, and B. H. Kahn, 2020: Improved Detection of Interannual Cloud
944 Variability over the Southern Hemisphere Using Legacy Satellites. *Journal of*
945 *Climate*, **33**, 8225–8236, <https://doi.org/10.1175/JCLI-D-19-0758.1>.
- 946 Lorenz, D. J., and D. L. Hartmann, 2001: Eddy–Zonal Flow Feedback in the Southern
947 Hemisphere. *Journal of the Atmospheric Sciences*, **58**, 3312–3327,
948 [https://doi.org/10.1175/1520-0469\(2001\)058<3312:EZZFFIT>2.0.CO;2](https://doi.org/10.1175/1520-0469(2001)058<3312:EZZFFIT>2.0.CO;2).
- 949 Lorenz, D. J. (2023). A Simple Mechanistic Model of Wave–Mean Flow Feedbacks,
950 Poleward Jet Shifts, and the Annular Mode. *Journal of the Atmospheric Sciences*,
951 **80**(2), 549–568. <https://doi.org/10.1175/JAS-D-22-0056.1>
- 952 Lu, J., B. E. Harrop, S. Lubis, S. Smith, G. Chen, and L. R. Leung, 2023: The role of cloud
953 radiative feedback in the propagating Southern Annular Mode. *Geophysical Research*
954 *Letters*. Submitted.
- 955 Lubis, S. W., and P. Hassanzadeh, 2020: An Eddy–Zonal Flow Feedback Model for
956 Propagating Annular Modes. *Journal of the Atmospheric Sciences*, **78**, 249–267,
957 <https://doi.org/10.1175/JAS-D-20-0214.1>.
- 958 Lutsko, N. J., and M. C. Hell, 2021: Moisture and the Persistence of Annular Modes. *Journal*
959 *of the Atmospheric Sciences*, **1**, <https://doi.org/10.1175/JAS-D-21-0055.1>.

- 960 Ma, D., P. Hassanzadeh, and Z. Kuang, 2017: Quantifying the Eddy–Jet Feedback Strength
961 of the Annular Mode in an Idealized GCM and Reanalysis Data. *Journal of the*
962 *Atmospheric Sciences*, **74**, 393–407, <https://doi.org/10.1175/JAS-D-16-0157.1>.
- 963 Nakamura, N., and A. Solomon, 2010: Finite-Amplitude Wave Activity and Mean Flow
964 Adjustments in the Atmospheric General Circulation. Part I: Quasigeostrophic Theory
965 and Analysis. *Journal of the Atmospheric Sciences*, **67**, 3967–3983,
966 <https://doi.org/10.1175/2010jas3503.1>.
- 967 ——, and D. Zhu, 2010: Finite-Amplitude Wave Activity and Diffusive Flux of Potential
968 Vorticity in Eddy–Mean Flow Interaction. *Journal of the Atmospheric Sciences*, **67**,
969 2701–2716, <https://doi.org/10.1175/2010jas3432.1>.
- 970 ——, and C. S. Y. Huang, 2017: Local Wave Activity and the Onset of Blocking along a
971 Potential Vorticity Front. *Journal of the Atmospheric Sciences*, **74**, 2341–2362,
972 <https://doi.org/10.1175/jas-d-17-0029.1>.
- 973 ——, 2018: Atmospheric blocking as a traffic jam in the jet stream. *Science*, 361(6397), 42–
974 47. <https://doi.org/10.1126/science.aat0721>
- 975 Nie, Y., Y. Zhang, G. Chen, X.-Q. Yang, and D. A. Burrows, 2014: Quantifying barotropic
976 and baroclinic eddy feedbacks in the persistence of the Southern Annular Mode.
977 *Geophysical Research Letters*, **41**, 8636–8644,
978 <https://doi.org/10.1002/2014GL062210>.
- 979 Palipane, E., J. Lu, P. Staten, G. Chen, and E. K. Schneider, 2017: Investigating the zonal
980 wind response to SST warming using transient ensemble AGCM experiments.
981 *Climate Dynamics*, **48**, 523–540, <https://doi.org/10.1007/s00382-016-3092-9>.
- 982 Papavasileiou, G., A. Voigt, and P. Knippertz, 2020: The role of observed cloud-radiative
983 anomalies for the dynamics of the North Atlantic Oscillation on synoptic time-scales.
984 *Quarterly Journal of the Royal Meteorological Society*, **146**, 1822–1841,
985 <https://doi.org/10.1002/qj.3768>.
- 986 Riehl, H., T. C. Yeh, and N. E. L. Seur, 1950: A Study of Variations of the General
987 Circulation. *Journal of the Atmospheric Sciences*, **7**, 181–194,
988 [https://doi.org/10.1175/1520-0469\(1950\)007<0181:ASOVOT>2.0.CO;2](https://doi.org/10.1175/1520-0469(1950)007<0181:ASOVOT>2.0.CO;2).
- 989 Ring, M. J., and R. A. Plumb, 2008: The Response of a Simplified GCM to Axisymmetric
990 Forcings: Applicability of the Fluctuation–Dissipation Theorem. *Journal of the*
991 *Atmospheric Sciences*, **65**, 3880–3898, <https://doi.org/10.1175/2008JAS2773.1>.

- 992 Robinson, W. A., 2000: A Baroclinic Mechanism for the Eddy Feedback on the Zonal Index.
993 *Journal of the Atmospheric Sciences*, **57**, 415–422, [https://doi.org/10.1175/1520-0469\(2000\)057<0415:ABMFTE>2.0.CO;2](https://doi.org/10.1175/1520-0469(2000)057<0415:ABMFTE>2.0.CO;2).
- 994 Saggioro, E., and T. G. Shepherd, 2019: Quantifying the Timescale and Strength of Southern
995 Hemisphere Intraseasonal Stratosphere-troposphere Coupling. *Geophysical Research
996 Letters*, **46**, 13479–13487, <https://doi.org/10.1029/2019GL084763>.
- 997 Sheshadri, A., and R. A. Plumb, 2017: Propagating Annular Modes: Empirical Orthogonal
998 Functions, Principal Oscillation Patterns, and Time Scales. *Journal of the
Atmospheric Sciences*, **74**, 1345–1361, <https://doi.org/10.1175/JAS-D-16-0291.1>.
- 1000 Simpson, I. R., and L. M. Polvani, 2016: Revisiting the relationship between jet position,
1001 forced response, and annular mode variability in the southern midlatitudes.
1002 *Geophysical Research Letters*, **43**, 2896–2903,
1003 <https://doi.org/10.1002/2016GL067989>.
- 1004 ——, T. G. Shepherd, P. Hitchcock, and J. F. Scinocca, 2013: Southern Annular Mode
1005 Dynamics in Observations and Models. Part II: Eddy Feedbacks. *Journal of Climate*,
1006 **26**, 5220–5241, <https://doi.org/10.1175/JCLI-D-12-00495.1>.
- 1007 Smith, S., P. W. Staten, and J. Lu, 2021: How Moist and Dry Intrusions Control the Local
1008 Hydrologic Cycle in Present and Future Climates. *Journal of Climate*, **34**, 4343–4359,
1009 <https://doi.org/10.1175/JCLI-D-20-0780.1>.
- 1010 Son, S.-W., and S. Lee, 2006: Preferred Modes of Variability and Their Relationship with
1011 Climate Change. *Journal of Climate*, **19**, 2063–2075,
1012 <https://doi.org/10.1175/JCLI3705.1>.
- 1013 Sparrow, S., M. Blackburn, and J. D. Haigh, 2009: Annular Variability and Eddy–Zonal Flow
1014 Interactions in a Simplified Atmospheric GCM. Part I: Characterization of High- and
1015 Low-Frequency Behavior. *Journal of the Atmospheric Sciences*, **66**, 3075–3094,
1016 <https://doi.org/10.1175/2009JAS2953.1>.
- 1017 Thompson, D. W. J., and J. M. Wallace, 2000: Annular Modes in the Extratropical
1018 Circulation. Part I: Month-to-Month Variability. *Journal of Climate*, **13**, 1000–1016,
1019 [https://doi.org/10.1175/1520-0442\(2000\)013<1000:AMITEC>2.0.CO;2](https://doi.org/10.1175/1520-0442(2000)013<1000:AMITEC>2.0.CO;2).
- 1020 ——, ——, and G. C. Hegerl, 2000: Annular Modes in the Extratropical Circulation. Part II:
1021 Trends. *Journal of Climate*, **13**, 1018–1036, [https://doi.org/10.1175/1520-0442\(2000\)013<1018:AMITEC>2.0.CO;2](https://doi.org/10.1175/1520-0442(2000)013<1018:AMITEC>2.0.CO;2).
- 1022
- 1023

- 1024 Wang, L., and N. Nakamura, 2015: Covariation of finite-amplitude wave activity and the
1025 zonal mean flow in the midlatitude troposphere: 1. Theory and application to the
1026 Southern Hemisphere summer. *Geophysical Research Letters*, **42**, 8192–8200,
1027 <https://doi.org/10.1002/2015gl065830>.
- 1028 Woollings, T., L. Papritz, C. Mbengue, and T. Spengler, 2016: Diabatic heating and jet
1029 stream shifts: A case study of the 2010 negative North Atlantic Oscillation winter.
1030 *Geophysical Research Letters*, **43**, 9994–10,002,
1031 <https://doi.org/10.1002/2016GL070146>.
- 1032 Xia, X., and E. K. M. Chang, 2014: Diabatic Damping of Zonal Index Variations. *Journal of*
1033 *the Atmospheric Sciences*, **71**, 3090–3105, <https://doi.org/10.1175/JAS-D-13-0292.1>.
- 1034 Zurita-Gotor, P., J. Blanco-Fuentes, and E. P. Gerber, 2014: The Impact of Baroclinic Eddy
1035 Feedback on the Persistence of Jet Variability in the Two-Layer Model. *Journal of the*
1036 *Atmospheric Sciences*, **71**, 410–429, <https://doi.org/10.1175/JAS-D-13-0102.1>.

Diabatic Eddy Forcing Increases Persistence and Opposes Propagation of the
Southern Annular Mode in MERRA2

Supplemental Materials

Samuel Smith^{1*}, Jian Lu², Paul W. Staten¹

¹Indiana University, Bloomington, IN

²Pacific Northwest National Laboratory, Richland, WA

*Contact information: samjsmit@iu.edu

Scaling of Diabatic FAWA Source

Beginning with the definition of the vertically-integrated diabatic heat source (c.f. Eq. (5) in the main text), using the alternative but equivalent definition of the FAWA integral (see Huang and Nakamura 2016)

$$\Delta\Sigma \equiv -\frac{a}{2\pi \cos \phi_e} \int_{p_b}^{p_t} \int_0^{2\pi} \int_0^{\Delta\phi} f \frac{\partial}{\partial p} \left(\frac{\dot{\theta}_d}{d\tilde{\theta}/dp} \right) \cos \phi d\lambda d\phi' dp. \quad (S1)$$

Here we introduce $\dot{\theta}_d \equiv (p_R p^{-1})^\kappa c_p^{-1} J_T$ which is the potential temperature tendency due to diabatic heat release. As in Huang and Nakamura (2016, hereafter HN16), ϕ' coordinates are a variable of integration between the equivalent latitude ϕ_e and the Q contour. $\Delta\phi(\lambda, \phi, \phi', p)$ can be multivalued, e.g., in the case of a cutoff low. See HN16 for more details.

We aim to simplify (S1) to build a physical intuition for how diabatic heating interacts with the mean flow in the FAWA framework. We make a series of assumptions to do this; these assumptions are not expected to provide accurate numerical computation of Eq. (S1), as numerical computation is done using Eq. (5). Rather, we only aim for a scaling which follows the general form of Eq. (S1).

First, we assume that the upper-level waves are relatively barotropic such that $\Delta\phi$ has relatively weak dependence on height, so that we can move the vertical integral in Eq. (S1) to the innermost position and eliminate it using the fundamental theorem of calculus

$$\Delta\Sigma \sim -\frac{a}{2\pi \cos \phi_e} \int_0^{2\pi} \int_0^{\Delta\phi} f \left(\frac{\dot{\theta}_d}{d\tilde{\theta}/dp} \right)_{p_b}^{p_t} \cos \phi d\lambda d\phi'. \quad (S2)$$

Next, we make use of the relationship that FAWA scales as $A \sim a\Delta\phi(q - Q) \equiv \eta q_e$ (see Nakamura and Zhu 2010, HN16, and Smith et al. 2021), where η is the cartesian length of the Q contour displacement, proportional to the meridional eddy stirring scale, and q_e is an eddy PV anomaly (the integrand in the FAWA calculation). In the same vein, we assume the innermost integral in Eq. (S2) should scale similarly, with the ratio $\frac{\cos \phi}{\cos \phi_e} \sim 1$

$$\Delta\Sigma \sim -\frac{1}{2\pi} \int_0^{2\pi} \eta f \left(\frac{\dot{\theta}'_d}{d\tilde{\theta}/dp} \right)_{p_b}^{p_t} d\lambda \quad (S3)$$

Note here the introduction of the prime on $\dot{\theta}_d$ to indicate the heating is an eddy term similar to q_e . Finally, we contend that $\dot{\theta}'_d \sim \Delta\theta'_d(\tau)^{-1}$, where $\Delta\theta'_d$ is the diabatic adjustment to potential temperature within an eddy during its lifetime, and τ is the eddy lifetime. Thus, we can approximate $\eta\tau^{-1} \sim v'_\tau$ as a kind of meridional transport velocity by midlatitude eddies, enabling a final simplification of Eq. (S3)

$$\Delta\Sigma \sim -f \left(\frac{\overline{v'_\tau \Delta\theta'_d}}{d\tilde{\theta}/dp} \right)_{p_b}^{p_t} \quad (S4)$$

Compare Eq. (S4) to the baroclinic term in Eq. (6) in the main text

$$-f \left(\frac{\overline{v'_g \theta'}}{d\tilde{\theta}/dp} \right) \Big|_{500}.$$

Thus, Eq. (S4) suggests that diabatic heating injects momentum into the mean flow in a similar process to the baroclinic injection performed by the vertical component of the Eliassen-Palm flux.

Supplemental Figures

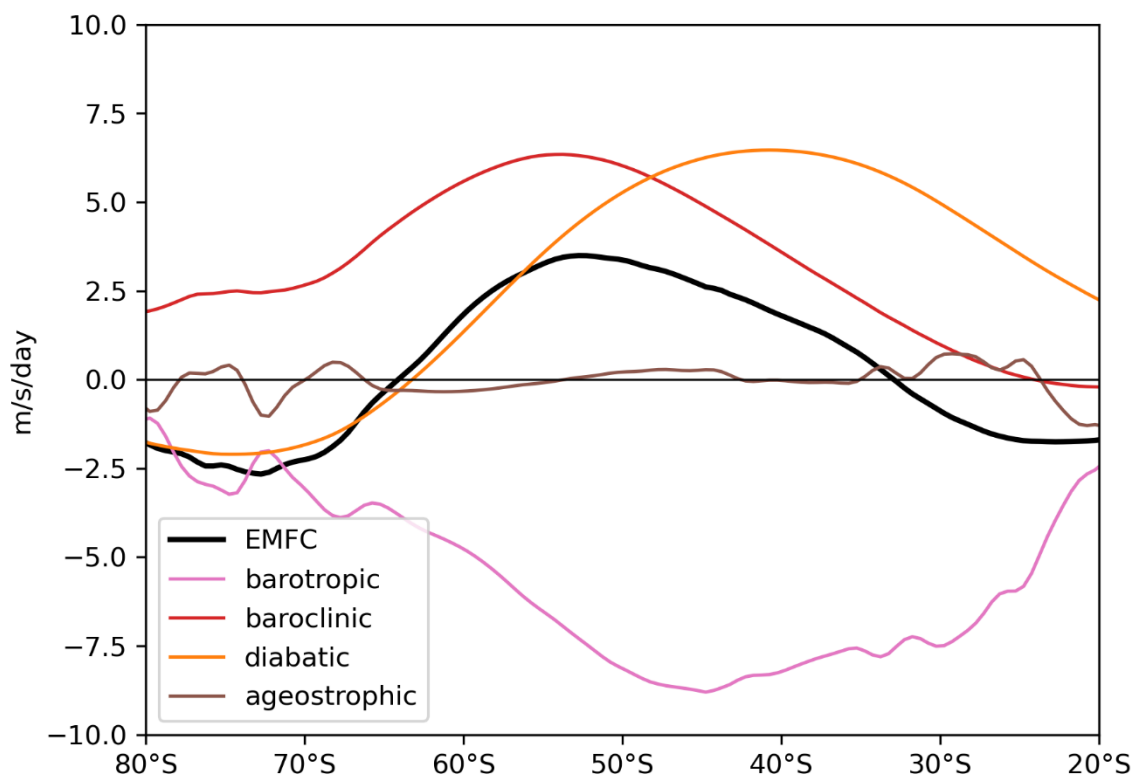


Figure S1: The climatological-mean partitioning of EMFC using the FAWA budget from MERRA2 data, 2005-2019. See Eq. 8 for more details. Note that the barotropic term is computed residually.

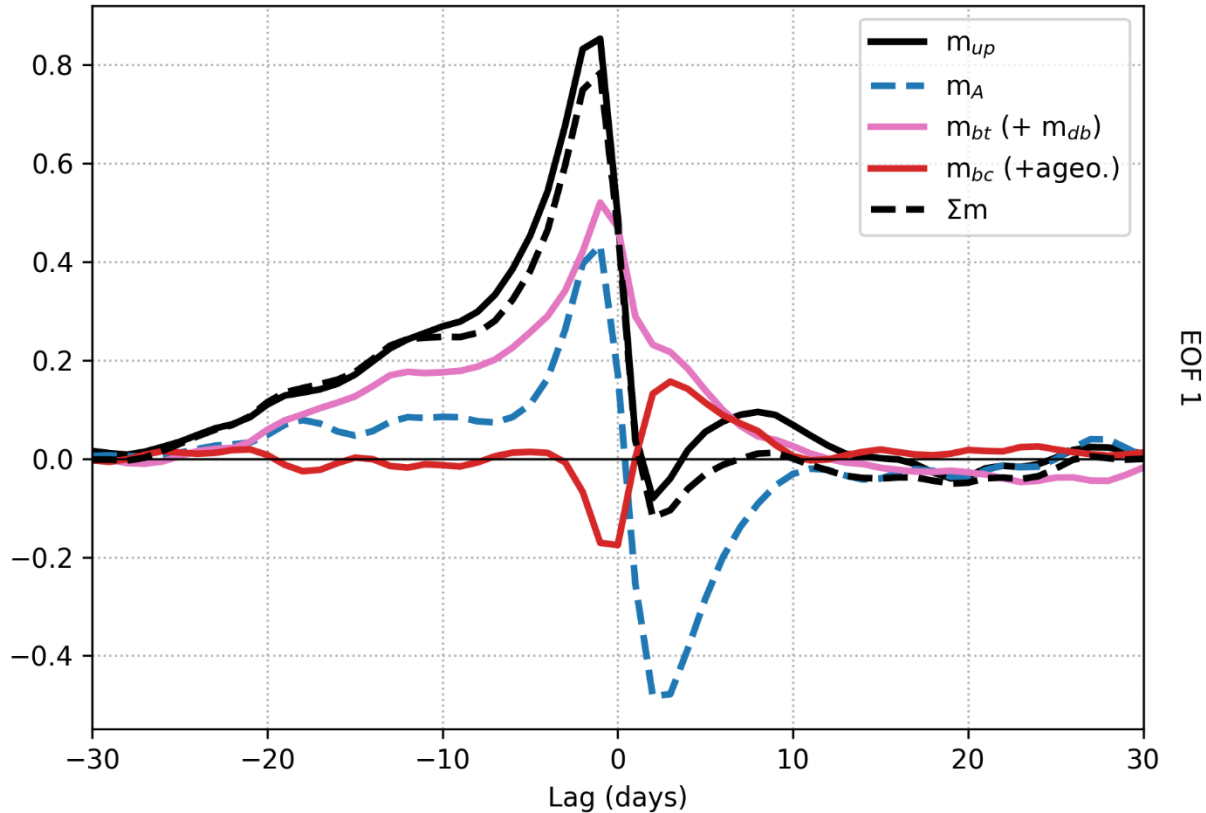


Figure S2: As in Figure 2, but in the style of Nie et al. (2014; see their Figure 2a)'s budget of the eddy momentum flux convergence, produced using the year-round MERRA2 data from 2005-2019 used for this study, only for EOF1. To match the magnitudes obtained by Nie et al. (2014), we down-sample the 6-hourly data to daily, while also coarsening the latitudinal resolution from 0.5° to 2.5° since the magnitude of a linear projection is sensitive to the horizontal resolution (see section 4.1). The PC index is taken to vary from -1 to 1 instead of having unit variance. Finally, we combine $m_{db} + m_{bt}$ for m_{bt} and take the full eddy heat flux rather than just the geostrophic for m_{bc} (see section 2.1).

SAM momentum

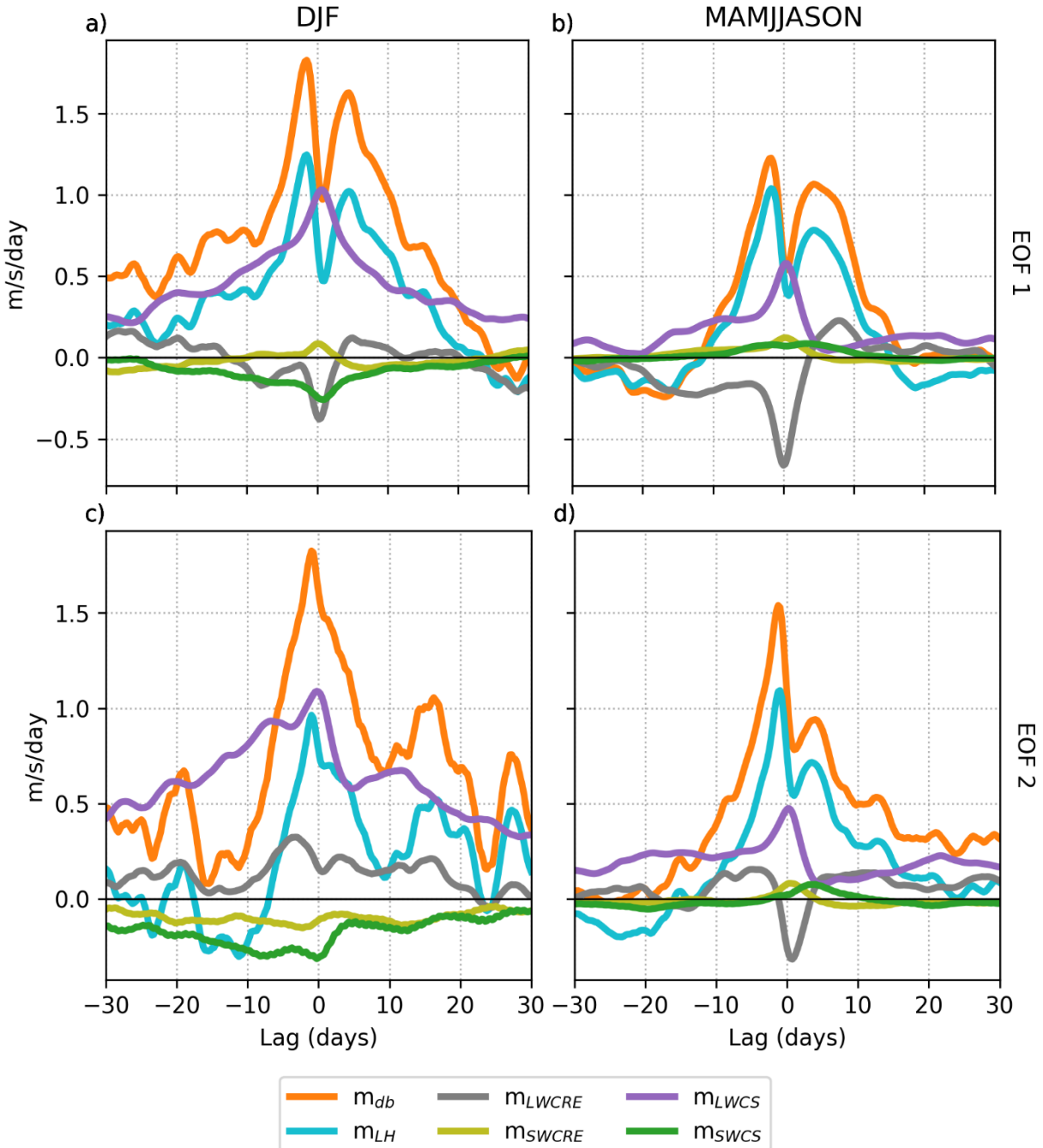


Figure S3: As in Figure 5, but including shortwave cloud (m_{SWCRE}) and clear-sky (m_{SWCS}) contributions, which are included in the total (m_{db}). Decompositions into cyclonic and anticyclonic contributions are not shown.

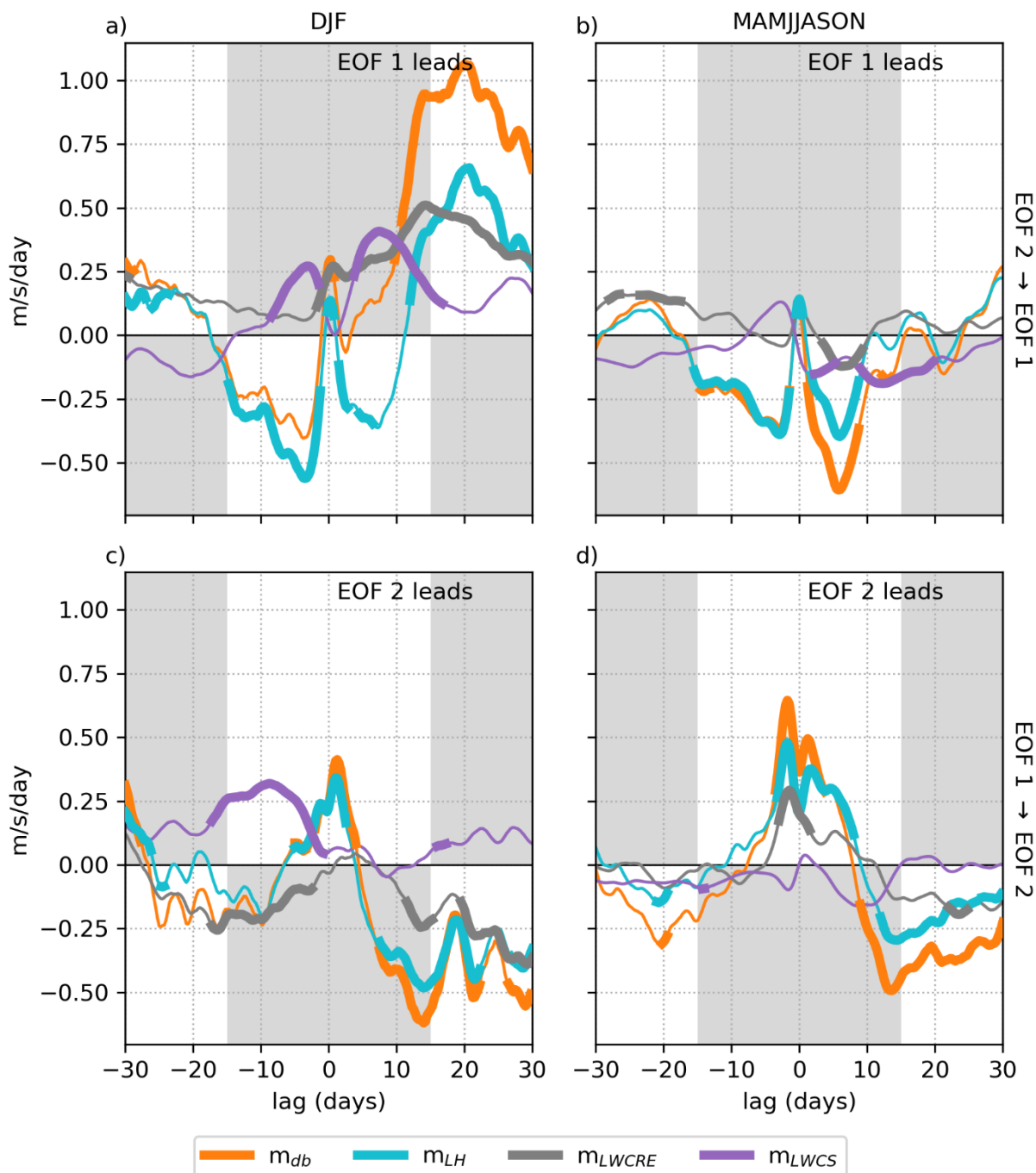


Figure S4: As in Figure 3a-d, but for each diabatic process separately (as in Figure 5).

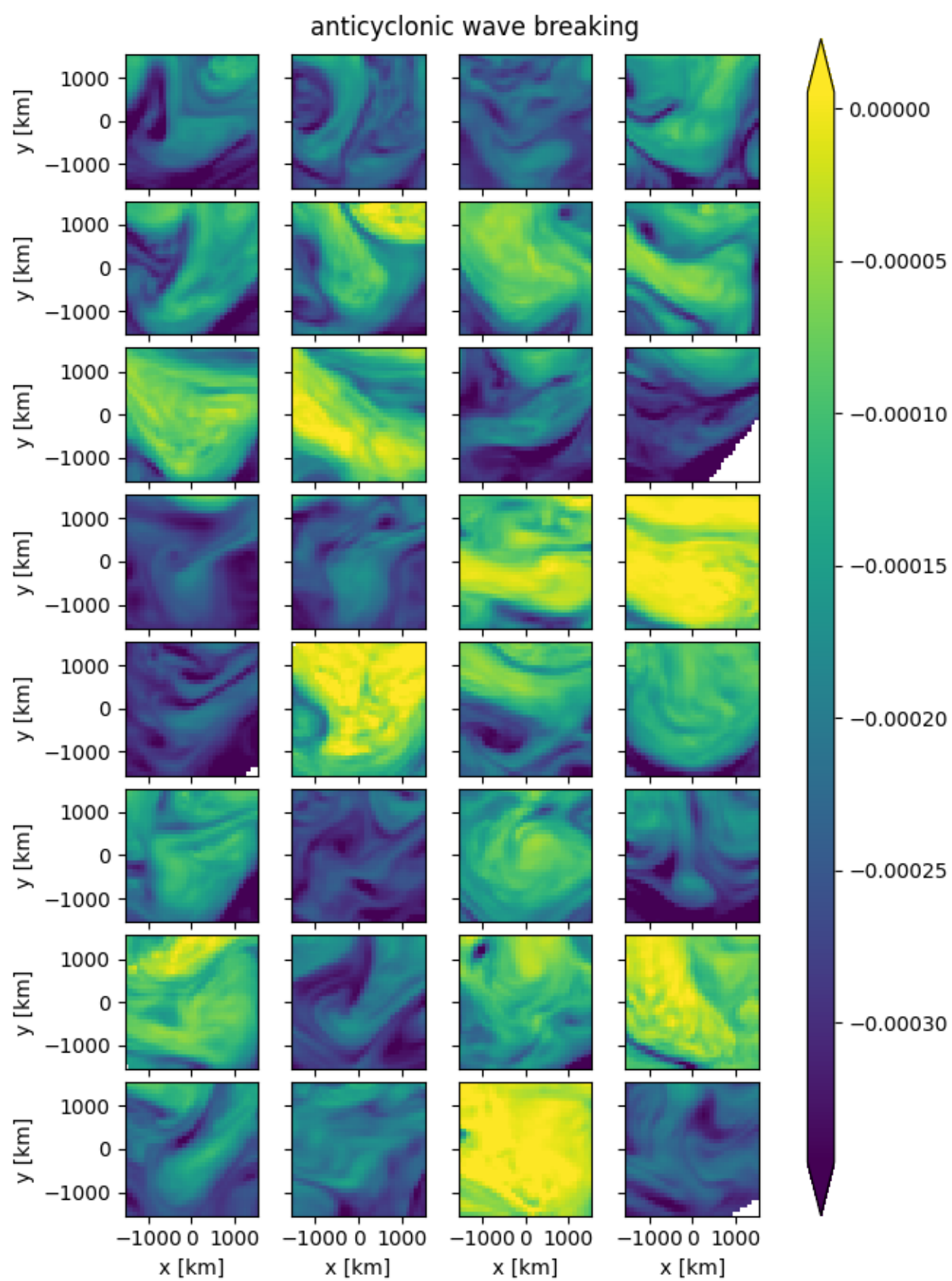


Figure S5: A random sample of anticyclonic wave breaking events identified by the wave activity tracking procedure described in section 3.2 for MERRA2 from 2005-2019. Shading is quasi-geostrophic potential vorticity taken at the same time and with the same central latitude/longitude as identified in the wave activity field. The x-coordinate is positive eastward, and the y-coordinate is positive northward. Missing values result when the data is too close to the pole to be properly interpolated.

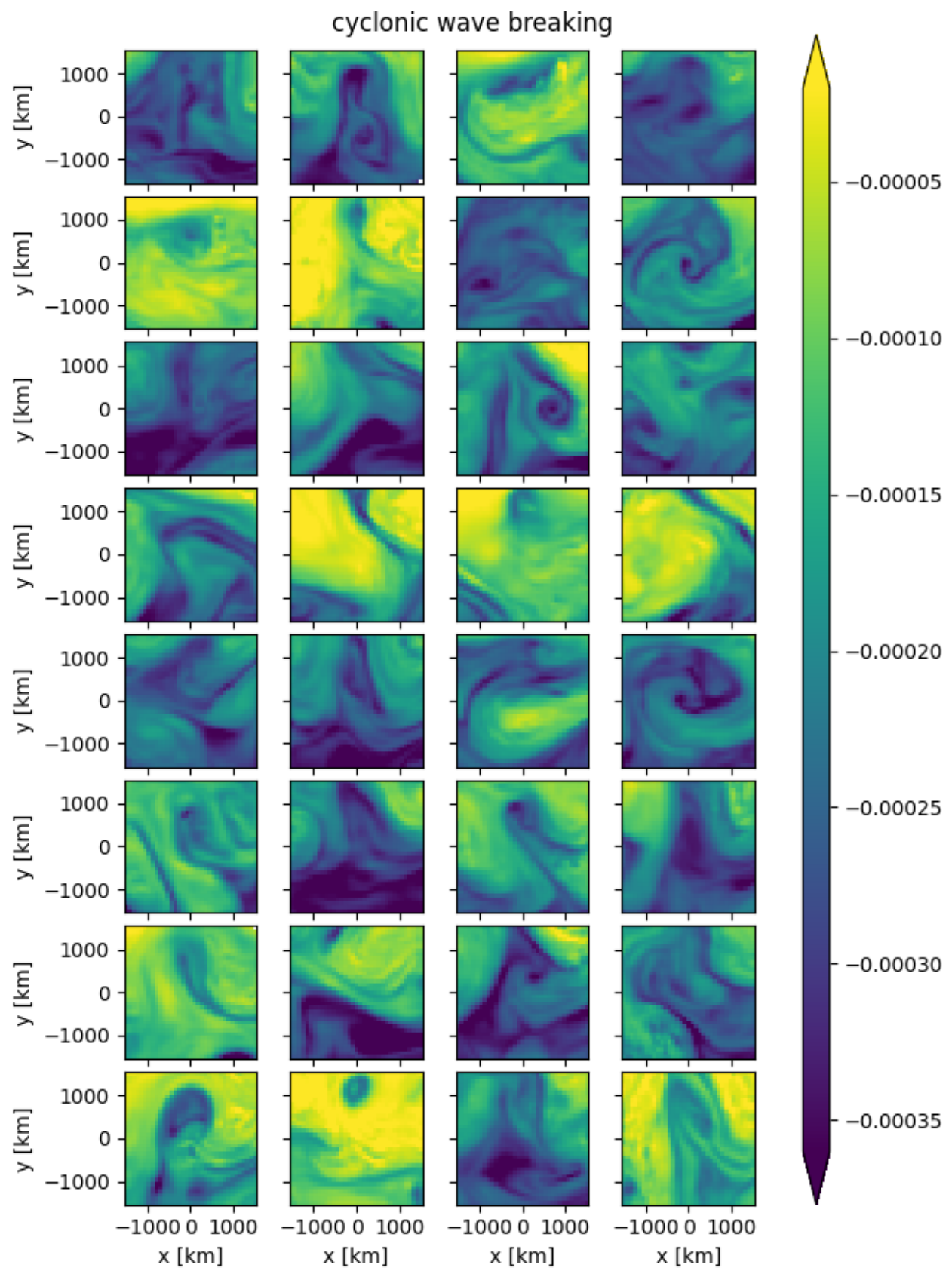


Figure S6: As in Figure S3, but for cyclonic wave breaking events.

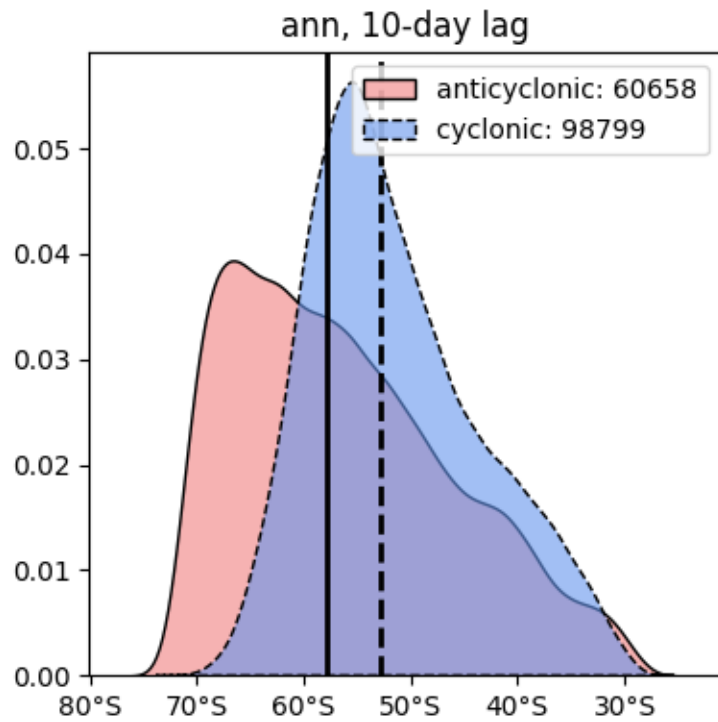


Figure S7: Probability distribution functions (PDFs) showing the counts and distribution of cyclone and anticyclone central latitudes in MERRA2 (2005-2019) identified using the method outlined in section 3.2. Distributions are year-round and for cyclones/anticyclones used in the 10-day lagged analysis of section 4.3. Black vertical lines represent the medians for the anticyclonic (solid) and cyclonic (dashed) waves. Note that latitudes are technically equivalent latitudes (c.f. Huang and Nakamura, 2016).